arXiv:1609.09376v1 [astro-ph.IM] 29 Sep 2016

Antennas and Receivers in Radio Interferometry

Todd R. Hunter[1] and Peter J. Napier[2]

[1]*NRAO, Charlottesville, VA, USA;* thunter@nrao.edu

[2]*NRAO, Socorro, VA, USA;* pnapier@nrao.edu

Abstract.
The primary antenna elements and receivers are two of the most important components in a synthesis telescope. Together they are responsible for locking onto an astronomical source in both direction and frequency, capturing its radiation, and converting it into signals suitable for digitization and correlation. The properties and performance of antennas and receivers can affect the quality of the synthesized images in a number of fundamental ways. In this lecture, their most relevant design and performance parameters are reviewed, with emphasis on the current ALMA and VLA systems. We discuss in detail the shape of the primary beam and the components of aperture efficiency, and we present the basics of holography, pointing, and servo control. On receivers, we outline the use of amplifiers and mixers both in the cryogenic front-end and in the room temperature back-end signal path. The essential properties of precision local oscillators (LOs), phase lock loops (PLLs), and LO modulation techniques are also described. We provide a demonstration of the method used during ALMA observations to measure the receiver and system sensitivity as a function of frequency. Finally, we offer a brief derivation and numerical simulation of the radiometer equation.

1. Introduction

In this lecture, we present the most important aspects of the antenna and receiver components of synthesis telescopes. Due to the increased breadth of material, we cannot cover all of the topics contained in the previous version of the summer school chapter on antennas (Napier 1999), in particular the section on antenna polarization properties. Instead, we review the basics of antennas while adding new details of interest to astronomers on the Atacama Large Millimeter/submillimeter Array (ALMA) and the Karl G. Jansky Very Large Array (VLA) dish reflectors. We follow with an overview of the heterodyne receiver systems and the receiver calibration techniques in use at these telescopes.

Figure 1 shows a simple block diagram of the major components required in an synthesis telescope. The role of the primary antenna elements of an interferometer is much the same as in any single element telescope: to track and capture radiation from a celestial object over a broad collecting area and focus and couple this signal into a receiver so that it can be detected, digitized and analyzed. At the output of the receiver feed, the signal is at the radio, or sky, frequency $\nu_{\rm RF}$, typically with a significant bandwidth $\Delta\nu$. The signal undergoes frequency translations and filtering as it propagates through the electronics system. In synthesis telescopes of recent design,

the analog signal processing and digitization systems are located in the antennas, with the resulting digital data transmitted over fiber optic cables to the correlator building. In general, the receiver, intermediate frequency, transmission cables, LO, and baseband portions of the electronics system all have the requirement of good amplitude and phase stability. These requirements and others such as stable bandpass shape, low spurious signal generation, and good signal isolation are discussed in Thompson et al. (2007) and in the ALMA and EVLA Memo series.

2. Antennas

Historically, a great variety of antenna types have been employed in synthesis telescopes (see the list in Napier et al. 1983, Table 1). In all cases, the diffraction beam of the primary antenna defines the solid angle over which an interferometer is sensitive, and is called the *primary beam*. The details of this angular response pattern, including beam shape, sidelobe level, and polarization purity, as well as how accurately it can track the target are important, and will directly affect the observed data.

2.1. Antenna types

The three major categories of antennas used in radio astronomy include: simple dipole antennas, horn antennas, and parabolic reflecting antennas. Dipole antennas provide the widest field response but at low gain, meaning that large arrays of hundreds or thousands of them are necessary to form beams with any reasonable level of resolution and sensitivity. They are typically used at wavelengths longer than 1 m, such as in the Long Wavelength Array (LWA, Ellingson et al. 2009). Horn antennas provide the most well-controlled beam shape and uniformity of response vs. frequency. Indeed, a hybrid of the horn and parabolic reflecting antenna types, the Crawford Hill horn-reflector (Crawford, Hogg & Hunt 1961), yielded the first detection of the cosmic microwave background (Penzias & Wilson 1965). Horn antennas have been combined into small interferometric arrays built on tracking platforms such as the Degree Angular Scale Interferometer (Halverson et al. 2002). However, horn antennas are not practical when a large collecting area is required because large single elements would be long, heavy, and difficult to arrange into a compact configuration. The reflecting dish antenna provides both good sensitivity and beam performance in its single element form, while being amenable to arrangement into reconfigurable interferometric arrays. In order to access a wide frequency range, many different receiver bands must be arranged with some mechanism to share the focal plane. However, this issue has been solved by a variety of approaches. For example, at the Green Bank Telescope (GBT, Prestage et al. 2009), up to eight receivers are mounted on a circular carriage which can rotate the selected receiver onto the focal axis. Because ALMA, VLA and many other major interferometers employ symmetric dish antennas with circular apertures, we will concentrate the rest of this section on this style of antenna.

2.2. Design of reflector antennas

Since the mid-1960's, reflector antennas have been designed using the principle of homology (von Hoerner 1967). Rather than trying to build a structure to resist the deformation associated with changes in orientation, a homologous design responds to the changes by allowing the surface to perturb from one parabola to another. This change

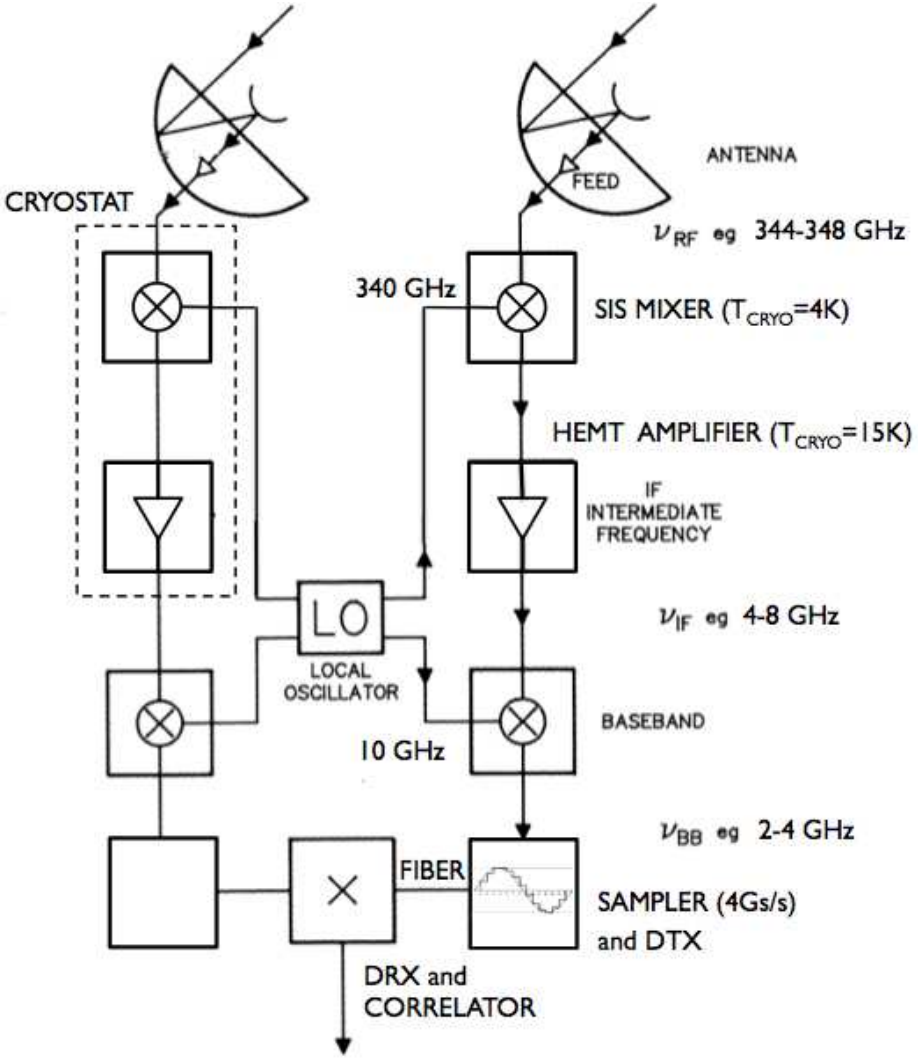

Figure 1. A simplified block diagram of the electronic equipment used to produce the correlation from one antenna pair in a synthesis telescope. The signal frequencies given as examples at various points through the electronics chain are typical of ALMA observing in Band 7 (LO1=340 GHz), but only one of the four dual-polarization basebands and samplers is shown (LO2=10 GHz). The digital transmitter (DTX) and digital receiver (DRX) relay the sampled data from the antenna to the central building via optical fiber. For lower frequency interferometers (like the VLA), the order of the first mixer and amplifier is swapped and the mixer is a room temperature device.

can then be compensated simply by applying a calibrated, concomitant motion (i.e. focus) of the subreflector. Further discussion on homology can be found in Baars (2007), which is an excellent reference on performance measurements techniques for parabolic reflector antennas. Structural engineering of antennas is discussed in Levy (1996). To summarize in a single sentence, the typical modern antenna presents a thin aluminum reflecting surface composed of dozens to hundreds of molded or machined segments

supported by a space frame backup structure (BUS) composed of carbon fiber reinforced (CFR) tubes and/or steel members and fasteners. These components promote high surface efficiency while offering some immunity to thermal deformation. The two major choices when designing a reflector antenna for use in a synthesis array are the choice of mount and the choice of optics.

For radio astronomy dishes, the alt-azimuth mount is the most prevalent in use today. Its advantages are its simplicity and the fact that gravity always acts on the reflector in the same plane, easing the challenge of a homologous design. The major disadvantage of this mount is that, as the antenna tracks, the aperture (and hence the primary beam) rotates with respect to the source, around the primary optical axis (Thompson et al. 2007). If the source size is significant compared to the beam size, and if the beam is not circularly symmetric, this rotation will cause the apparent brightness distribution to vary. Since aperture blockage usually makes the beam sidelobe pattern non-circularly symmetric, and the antenna instrumental polarization is not circularly symmetric, the dynamic range of total intensity images of very large sources and polarization images of extended sources will be limited by this effect. Observers of extended sources need to consider this effect when judging the fidelity of subtle features in the images of these sources. A minor disadvantage of the alt-az mount is that sources passing close to the zenith cannot be tracked well due to the high rates of azimuth rotation needed. Technically, the sidereal azimuth rate exceeds the (relatively slow) slew rate of the VLA and GBT ($\sim 40°$/minute) only for elevations $> 89.67°$. However, many antenna servos are not necessarily designed for smooth tracking at high rates, so errors may be larger (§ 2.7). Often of greater concern is the typically reduced accuracy of the pointing model at elevations $> 80°$ (§ 2.6).

There are a variety of optical systems that can be used to feed a large radio reflector (e.g. Rudge et al. 1982). Figure 2 shows the major types of feed systems that are in use on current radio telescope reflectors. The *prime focus system*, as in the Westerbork Synthesis Radio Telescope (WSRT, Baars & Hooghoudt 1974) and the Giant Meterwave Radio Telescope (GMRT, Ananthakrishnan 1995), has the advantage that it can be used over the full frequency range of the reflector, including the lowest frequencies where secondary focus feeds become impractically large. The disadvantages of the prime focus are that space for, and access to, the feed and receiver is restricted and spillover noise from the ground decreases sensitivity. All of the *multiple reflector systems* (Figure 2(b)–(f)) have the advantage of more space, easier access to the feed and receiver, and reduced noise pickup from the ground. In addition, the primary and secondary reflectors can be shaped to provide more uniform illumination in the main reflector aperture, as described in § 2.3. The *off-axis Cassegrain* (e.g., VLA, VLBA, ALMA) is particularly suitable for synthesis telescopes needing frequency flexibility, because many feeds can be located in a circle around the main reflector axis. Changing frequency simply requires either a rotation of the asymmetric subreflector around this axis, as in the VLA (Napier et al. 1983) and VLBA (Napier et al. 1994), or by adjusting the pointing of the primary mirror as in ALMA (Hills et al. 2010). The disadvantage of this geometry is that the asymmetry degrades polarization performance. The *Nasmyth geometry* (e.g., the 10.4 m Leighton dishes of the Combined Array for Millimeter Astronomy (CARMA), Woody et al. 2004) provides a receiver cabin external to the antenna structure, whilst the *bent Nasmyth geometry* (e.g., Submillimeter Array (SMA)) minimizes disturbances to the receivers because they (along with the final three mirrors) do not tilt in elevation (Paine et al. 1994). The bent Nasmyth geometry provides maximum convenience for service access, even during observations. Finally, the *dual*

offset Gregorian (e.g., GBT) has no blockage and thus delivers a circularly symmetric beam with low sidelobes which is particularly important for Galactic H I observations (Boothroyd et al. 2011). This characteristic makes it an attractive choice for wide field-of-view synthesis telescopes, but the increased complexity of reflector panel tooling and subreflector support structure leads to increased cost.

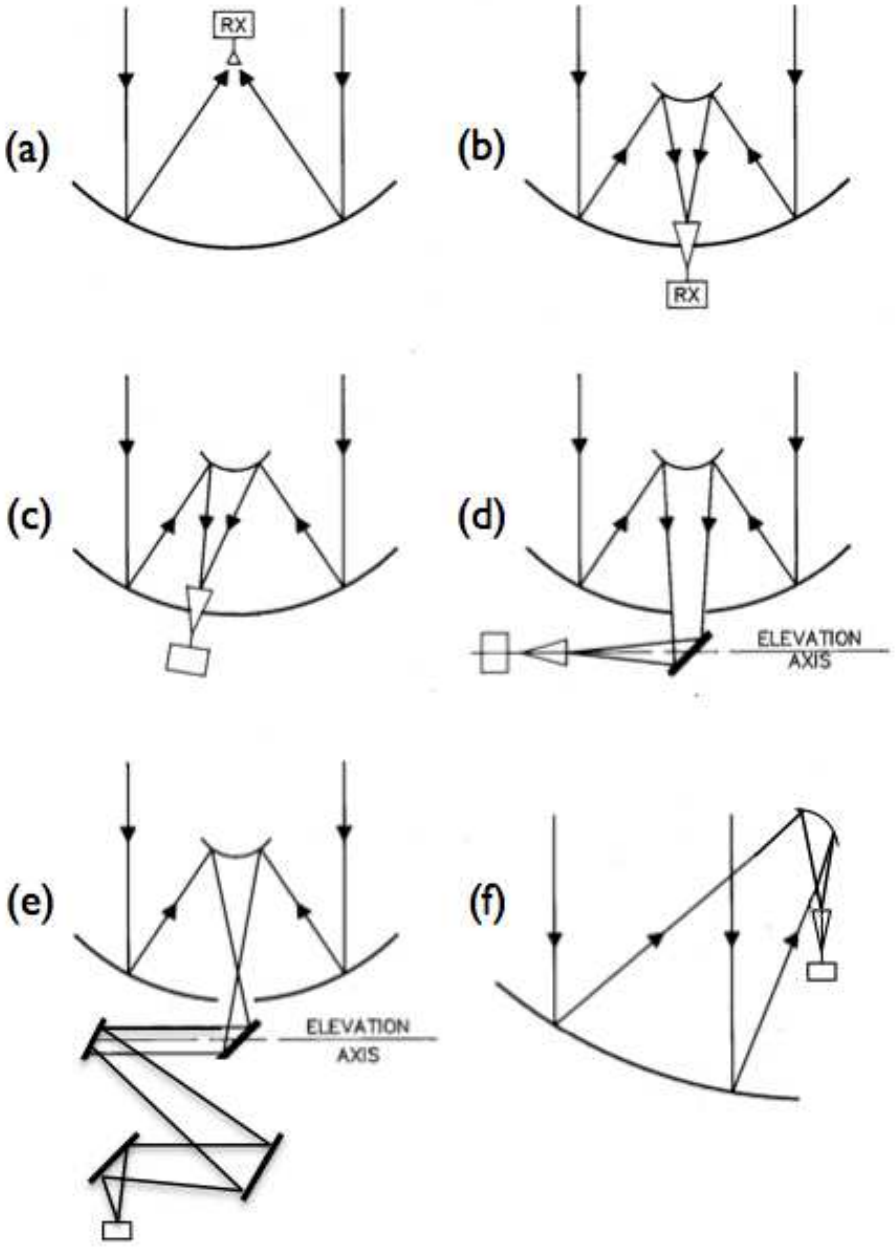

Figure 2. Optical systems for radio telescope reflectors. **(a)** Prime focus, **(b)** Cassegrain, **(c)** Off-axis Cassegrain, **(d)** Nasmyth, **(e)** Bent Nasmyth, **(f)** Dual offset Gregorian.

2.3. Antenna primary beam shape

As described in Napier (1999), there is a Fourier transform relationship between the complex voltage distribution of the electric field, $f(u,v)$, in the aperture of an antenna and the corresponding complex far-field voltage radiation pattern, $F(l,m)$ of the antenna (see also Kraus 1986, §6–8). In both domains, the power pattern is the square of the absolute magnitude of the voltage pattern. The form of $f(u,v)$ for an antenna is determined by the way in which the antenna feed illuminates the aperture. In general, the more that $f(u,v)$ is tapered at the edge of the aperture, the lower will be the aperture efficiency and the sidelobe response, and the broader the main beam. Calculations for a variety of $f(u,v)$, and their corresponding $F(l,m)$, can be found in antenna textbooks (e.g. Baars 2007, Chapter 4). Figure 3 shows one-dimensional cuts through $f(u,v)$ and $|F(l,m)|^2$ for uniform and tapered illumination patterns.

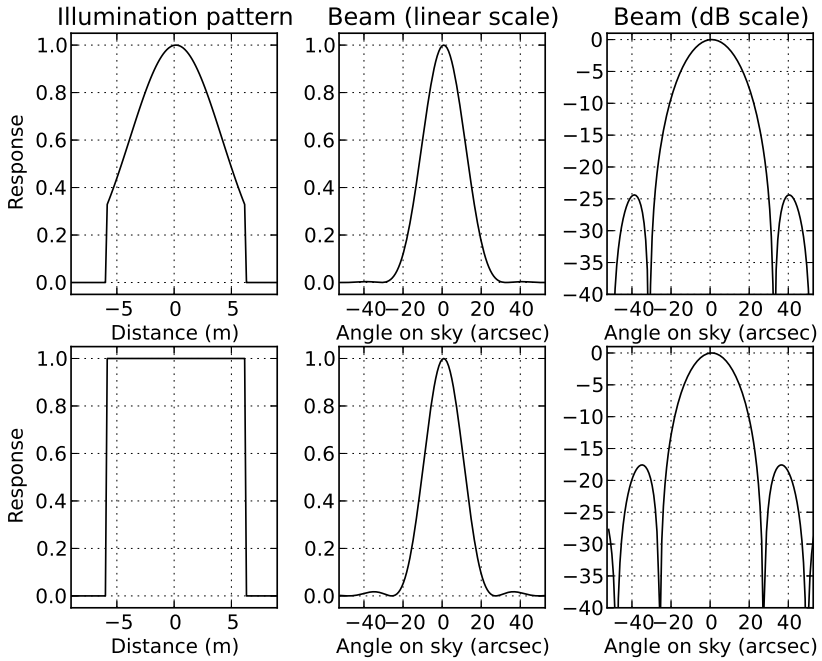

Figure 3. These plots are one-dimensional cuts through two-dimensional images simulating an (unblocked) 12 m diameter antenna observing at 230 GHz, showing the relationship between an antenna's aperture voltage pattern $f(u)$ (left column) and its far-field radiation power pattern $|F(l)|^2$ (right columns). The top row shows the case of a Gaussian edge taper (-10 dB in power) while the bottom row shows what would happen with uniform illumination. In general, both quantities are complex but only the amplitudes are shown here. Note the difference in beam width and sidelobe level.

In order to maximize sensitivity (at the expense of higher sidelobes), the VLA antennas were designed to have a nearly uniform illumination ($f(u,v)$ = constant) over the whole aperture, except where the aperture is blocked by the subreflector and its support struts. Because efficient receiver feedhorns have a tapered response, achieving this uniform illumination required mathematically perturbing the primary and secondary mirror

surfaces into complementary "shaped" surfaces (Williams 1965). In other words, the VLA antennas are **not** the classical Cassegrain combination of paraboloidal primary with hyperboloidal secondary. While the primary differs from a paraboloid by only 1 cm rms (Napier et al. 1983), recent optical modeling employed a polynomial of order 13 to accurately represent the surface (Srikanth et al. 2005). The VLBA antennas are similarly shaped to provide uniform illumination out to 95% of the dish radius, then tapered to -15 dB at the edge (Napier et al. 1994).

With uniform illumination, for a circularly symmetric aperture of diameter D, the beam pattern takes the form $F(u) = J_1(\pi Du)/u$, which has the following properties: first sidelobe level = -17.57 dB (i.e. $10^{-1.757}$ compared to the peak), half power beam width HPBW = $1.028\lambda/D$, and the radius of the first null = $1.22\lambda/D$. These values are in good agreement with measured beam parameters for the VLA 25 m diameter reflector, except for the first sidelobe level (about -16 dB), which is increased from theory by the aperture blockage. The VLA beam patterns in the various bands are characterized by sixth-order polynomial functions in the AIPS software package, and analytically by an Airy pattern (truncated at the 10% level) in the CASA software package. More accurate patterns are being added to CASA. Some disadvantages of shaped Cassegrain geometries, which do not usually preclude their use for synthesis telescopes, include compromised prime focus operation above a frequency of about 1 GHz because of the shaped main reflector (the VLBA 600 MHz system suffers 5% loss due to this effect), and very bad beam degradation if the feed is moved away from the secondary focal point. This latter problem can limit their use in synthesis arrays designed to obtain very wide fields of view by using focal plane arrays (FPAs). Note that the Apertif FPA system (Oosterloo et al. 2009), which has a $8^{\circ 2}$ field of view at 1.4 GHz, operates at prime focus on the WSRT whose 25 m antennas are paraboloidal in shape (Baars & Hooghoudt 1974) and thus do not suffer from this complication.

In contrast, ALMA antennas were designed to have a tapered illumination pattern because it provides reduced sidelobes which promotes better single dish imaging performance, a required capability of ALMA. In addition, the classical Cassegrain geometry provides good performance over a much larger area of the focal plane, which the stationary ALMA receivers must share. By specification, the taper of the receiver feeds at the edge of the subreflector is -12 dB in the Gaussian beam approximation, which equates to -10 dB in the physical optics analysis (Rudolf et al. 2007). A quadratic taper of -10 dB (i.e. the power at the edge of the dish is 10% of the peak) corresponds to a HPBW of $1.137\lambda/D$ (Baars 2007, Eq 4.13). The central obstruction of 0.75 m on the 12 m antennas produces a further $\sim$ 0.5% reduction in the beam pattern (Schroeder 1987) to a final HPBW of 1.13λ/D. The theoretical peak of the first sidelobe is -24 dB for an unblocked aperture. The effect of a central blockage is to increase the odd-numbered sidelobes by a few dB while similarly decreasing the even-numbered sidelobes. Currently in CASA, the ALMA beam pattern is an Airy pattern scaled to match the measured HPBW, i.e. the Airy pattern for a 10.7 m antenna is used for the 12 m antennas. An improved representation of the beam patterns from celestial holography measurements is currently under test.

When considering the effect of radio frequency interference (RFI), it is important to know the response in the far sidelobes, which has been measured on the VLA and VLBA antennas at $\lambda = 18$ cm (Dhawan 2002). The declining envelope of the sidelobe response is consistent with the reference radiation pattern for large diameter ($D/\lambda \geq 100$) parabolic Cassegrain antennas tabulated in Recommendation SA.509-3 of

the radiocommunication sector of the International Telecommunications Union (ITU-R 2013). In general, the gain relative to the main beam will drop below -60 dB somewhere between $10^\circ - 20^\circ$ off axis.

2.4. Antenna efficiencies

For antennas that have a well defined physical collecting area, such as reflector, lens or horn antennas, the ratio of the effective area A_0 to the physical area A of the aperture is called the aperture efficiency η, a dimensionless quantity less than unity:

$$\eta = A_0/A\,. \tag{1}$$

The antenna aperture efficiency directly impacts the sensitivity of the synthesis telescope and is the product of a number of different loss factors,

$$\eta = \eta_{\rm Ruze}\,\eta_{\rm bl}\,\eta_{\rm s}\,\eta_{\rm t}\,\eta_{\rm r}\,\eta_{\rm misc}\,, \tag{2}$$

where $\eta_{\rm Ruze}$ = reflector surface efficiency, $\eta_{\rm bl}$ = reflector blockage efficiency (feed legs and subreflector), $\eta_{\rm s}$ = feed spillover efficiency, $\eta_{\rm t}$ = illumination taper efficiency, $\eta_{\rm r}$ = panel reflection efficiency, and $\eta_{\rm misc}$ = miscellaneous efficiency losses due to reflector diffraction, feed position errors, and polarization efficiency. As we will see, the term that is the most frequency dependent is $\eta_{\rm Ruze}$. Hence, it is often the case that observatory documentation will define the aperture efficiency as $\eta_0\eta_{\rm Ruze}$ where η_0 is simply the product of all the other efficiencies. For example, the ALMA technical handbook[1] quotes $\eta_0 = 0.72$. It is important to realize that η is typically elevation-dependent, with the best values occurring at moderate elevations (usually between 45-60°). Gain curves showing η vs. elevation for the VLA antennas are stored in CASA (Figure 4) and can be used to correct for this varying amplitude response in the data.

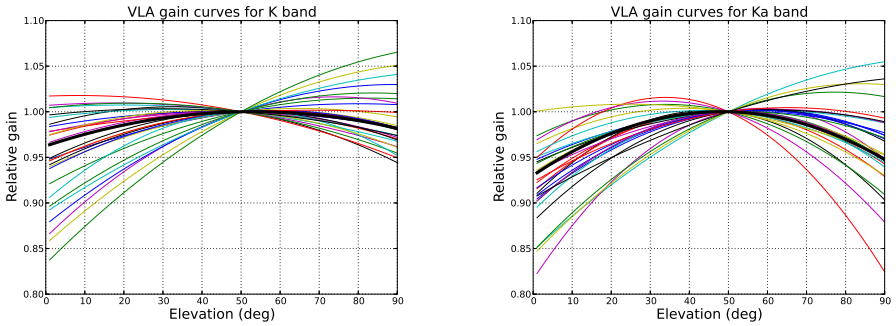

Figure 4. Gain curves stored in CASA for all the VLA K and K_a-band receivers as of December 2014 (all antennas overlaid). In each plot, the thick line is the mean curve.

[1] https://almascience.nrao.edu/documents-and-tools/cycle4/alma-technical-handbook

2.4.1. Surface efficiency

$\eta_{\rm Ruze}$ accounts for loss due to inaccuracies in the profile of the reflector. Surface errors cause the electric field from different parts of the aperture to not add together perfectly in phase at the feed, leading to a decrease in received power. Ruze (1966) gives an expression for surface efficiency

$$\eta_{\rm Ruze} = e^{-(4\pi\sigma/\lambda)^2} , \tag{3}$$

where σ is the rms surface error, with the errors assumed to be Gaussian random and uncorrelated across the aperture. In a Cassegrain (or more complicated) mirror system, σ is an appropriately defined composite rms error of the primary and secondary reflector surfaces, which should always dominate over subsequent (more accurate) smaller mirrors. If the errors are correlated over significant fractions of the aperture, then additional terms are required on the right hand side of Eq. 3, or more accurately, an integration of the surface profile map must be performed. Eq. 3 predicts that for an rms error of $\lambda/16$, $\eta_{\rm Ruze} = 0.54$, which is often taken to define the useful upper frequency limit ($\nu_{\rm upper}$) for a reflector. For the VLA, with $\sigma \approx 400\mu$m, $\lambda/16$ corresponds to $\nu_{\rm upper} = 47$ GHz. For ALMA, with $\sigma \approx 20\mu$m, $\nu_{\rm upper} = 940$ GHz. Most of the drop in $\eta_{\rm Ruze}$ occurs between 0.5-1.0$\nu_{\rm upper}$, as can be seen in Table 1.

As well as the loss of sensitivity resulting from a low value of $\eta_{\rm Ruze}$, one must be concerned with the quality of the primary beam. The surface errors cause scattering which produces a broad pedestal surrounding the main lobe of the beam that can be higher than the usual diffraction-limited sidelobes. This pedestal can enhance image artifacts caused by sources near the primary beam. For a reflector of diameter D, if the reflector errors are correlated over distances D/N then the scatter pattern will be N times broader than the diffraction-limited main lobe, and often correspond to the panel segment size. Measurements of this pattern can be made by scanning large objects like the Moon (Schwab & Hunter 2007; Greve et al. 1998). Good $\eta_{\rm Ruze}$ performance requires careful structural design for wind, thermal and gravitational loading, together with precise reflector panels (e.g. Bosma 1998; Ezawa et al. 2000) and an accurate panel setting technique (see § 2.5).

2.4.2. Blockage efficiency

The feed or subreflector and its multi-legged support structure block the aperture of a reflector antenna. This typically results in a blockage efficiency in the range $0.75 < \eta_{\rm bl} < 0.95$. A formula for $\eta_{\rm bl}$ is given (Lamb & Olver 1986) by

$$\eta_{\rm bl} = \left(1 - \frac{\text{effective blocked area}}{\text{total area}}\right)^2 . \tag{4}$$

The effective blocked area is the blocked area weighted for the illumination taper in the aperture (see also Goldsmith 2002). Similarly, the total area is weighted for the illumination taper in the aperture. Equation 4 shows, for small blockage, that the loss in efficiency is twice the fractional blocked area. As well as the loss in aperture efficiency, the increase in antenna beam sidelobe level due to blockage is important for synthesis telescopes. Using the Fourier transform relationship, the form of the antenna voltage pattern with blockage can be calculated as the unblocked voltage pattern minus the voltage patterns of the blocked areas. As a practical example, the ALMA 12 m antennas are of three different designs (Vertex, AEC and Melco, corresponding to the three

funding partners: North America, Europe, East Asia), and the effect of their different blockage can be seen in their respective beam patterns. The feedleg design of the AEC antennas is significantly different from the other two designs in that the four struts are mounted entirely from the edge of the dish (Figure 5). In contrast, the feed struts of the Vertex and Melco antennas meet the dish in several places along the outer half of the dish, meaning that scattering occurs twice–once on the way from the sky down to the primary mirror (plane wave scattering) and again on the way back up to the subreflector (spherical wave scattering). As shown in Figure 5, the first sidelobe is lower and more azimuthally uniform on the AEC antennas compared to the Vertex antennas.

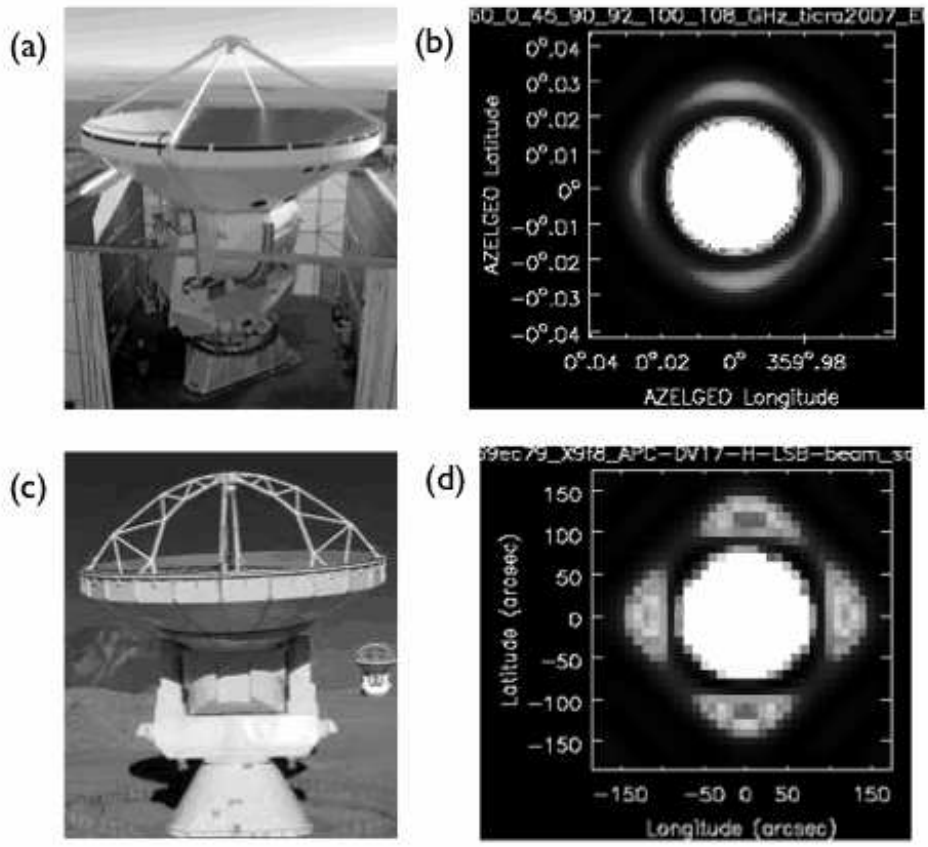

Figure 5. (a) Photograph of a 12 m ALMA AEC antenna whose feedlegs block only the plane wave from the sky; (b) 100 GHz amplitude beam pattern of an AEC antenna obtained from celestial holography; (c) Photograph of a 12 m ALMA Vertex antenna whose feedlegs also block the spherical wave (i.e., between the primary and secondary mirror); (d) beam pattern of a Vertex antenna. Note the differences in the first sidelobe due to the difference in feed leg geometry.

2.4.3. Feed spillover and illumination taper efficiency

These two efficiency terms are related to one another, and their product is sometimes (confusingly) referred to as the illumination efficiency. The spillover efficiency can

most easily be understood by considering the antenna in transmission, rather than reception mode. The spillover efficiency is the fraction of the power radiated by the feed that is intercepted by the subreflector for a Cassegrain feed, or by the main reflector for a prime focus system. Clearly, power that does not intercept the reflector is lost, and we can be confident that a similar loss occurs in reception mode by invoking the Reciprocity Principle (Rudge et al. 1982, p. 11). Simultaneously, the illumination taper efficiency arises whenever the outer parts of the antenna are illuminated at a lower power level than the central portion, and hence contribute lower "weight" in the aggregate signal (similar to applying a uv-taper in synthesis imaging). The spillover and taper efficiencies can be computed using the integral formulas given in Napier (1999); but in a qualitative sense, it should be obvious that adjusting the taper in one direction will generally improve one term at the expense of the other. For unshaped, classical Cassegrain systems (like ALMA antennas), the illumination taper that gives the best trade-off (i.e., -10 dB, Goldsmith 1987) will produce a spillover efficiency of ≈ 0.9, a taper efficiency of ≈ 0.9, and consequently, a net product of ≈ 0.8. By comparison, for the VLA antennas, whose illumination pattern is much closer to uniform, the net product is ≈ 0.9 (Napier et al. 1983).

2.4.4. Panel reflection efficiency

Aside from surface errors encompassed by the $\eta_{\rm Ruze}$ term, smooth unpainted aluminum surfaces generally have a very high reflectivity at centimeter through submillimeter wavelengths (typically ≥ 0.99 per mirror, Ezawa et al. 2000). Addition of paint, which provides long-term protection, adds a small amount of loss at centimeter frequencies due to additional scattering (up to a few percent, Lamb 1992). However, above 100 GHz the dissipative loss of the paint's dielectric material becomes significant, which is why the panels of most (sub)millimeter telescopes are left unpainted. Although unpainted, ALMA panels are slightly roughened in order to scatter infrared radiation to enable safe observations of the Sun.

2.4.5. Miscellaneous efficiencies

Not included in the previous efficiency terms is the effect of diffraction at each aperture. Whenever the focusing mirror diameters are large compared to the wavelength of observation, diffraction losses are low (a few percent or less). However, these losses become significant at the long wavelength end of many telescopes. For example, at 1 GHz, the diffraction efficiency of the VLA antennas is 0.85 (Napier et al. 1983).

The ideal amplitude response of the primary beam is circularly symmetric with respect to the optical axis, with constant phase out to the first null, and alternating by 180° in successive sidelobes. In reality, small errors in alignment of the subreflector with respect to the primary surface (i.e. focus errors) can produce a non-circular beam, which is accompanied by a reduction in efficiency (Butler 2003; Goldsmith 2002). Furthermore, any small errors in the alignment of the receiver feed with respect to the optical axis (termed an "illumination offset") produce non-uniform phase response in the outer portion of the main beam (Holdaway 2001). In addition to loss of efficiency, this effect can produce problems when imaging extended objects and may require special calibration if the misalignment is significant (Bhatnagar et al. 2008).

2.5. Surface setting techniques

Precision multi-panel reflectors are composed of individual panel segments typically with four or five screw adjustment points per panel. The initial setting of the surface segments is generally performed with a mechanical alignment device or theodolite-assisted technique, which can achieve accuracies of $\lesssim 1$ part in 10^5 of the total aperture diameter D. Further refinement is often done using photogrammetry (Kesteven 2012; Feng et al. 2010; Miller et al. 2003). This technique entails placing reflective tape targets on the corners of each panel, imaging the entire surface with a high resolution digital camera from various angles, and solving for the best fit surface profile. Applying manual surface adjustments based on this measured profile can typically reach accuracies of a few parts in 10^6 of D. The ultimate surface performance is usually achieved using microwave holography, a technique developed during the 1970's (Napier & Bates 1971; Bennett et al. 1976) and in use at nearly every radio through submillimeter observatory (e.g. Hunter et al. 2011a; Baars 2007; Baars et al. 1999; Grahl et al. 1986). In this context, the term holography refers to the process of mapping the complex (amplitude and phase) beam pattern of an antenna and Fourier transforming the data to the aperture plane. The angular extent of the map (typically $1-2^\circ$) determines the linear resolution on the dish. The phase map provides the surface deviations in units of the observed wavelength; thus, the wavelength sets the ultimate accuracy, but it is constrained by the available sources of radiation. Centimeter-wave telescopes typically use geosynchronous broadcast satellite signals in K_u band ($\lambda = 2.5$ cm), either their analog continuous wave beacons (i.e. spectral line observed with a narrowband filter) or their broadband digital transmissions. Continuum from bright quasars can also be used (Kesteven 1993; Padin et al. 1987). Millimeter-wave telescopes need higher precision (hence higher frequency sources) and typically use ground-based 3 mm transmitters mounted on towers, though wavelengths as short as 0.4 mm have been used (Sridharan et al. 2002).

With a well-tuned holography system, the measurement errors are typically about 0.5-1 part in 10^6 of D. In addition to measuring panel misalignment, holography can be used to measure illumination offsets (§ 2.4.5), systematic antenna panel mold error (Hunter et al. 2011a) as well as large-scale deformations due to thermal effects. Large-scale features can also be measured by celestial holography, in which bright maser lines (Morris et al. 1988) or quasar continuum emissions are used as the radiation source. A sidereal source provides the advantage that dish deformations can be measured at different elevations. All of these forms of traditional holography require a second stationary antenna as a reference signal. An alternative technique called "phase retrieval" or "out-of-focus" holography can be performed on a single antenna by mapping the amplitude beam and fitting for the associated phase error (Nikolic et al. 2007).

2.6. Pointing model and metrology

Each antenna in a synthesis array employs a pointing model which continuously converts the requested topocentric coordinates into the actual encoder coordinates that will put the antenna on-source. Pointing models account for basic effects such as encoder zero offsets, collimation error, non-perpendicularity of the axes, and pad tilt, as well as higher-order terms that account for gravitational flexure, encoder eccentricity and other mechanical asymmetries (e.g. Mangum et al. 2006; Patel & Sridharan 2004). Some antennas employ additional metrology, such as thermometers (GBT, Prestage et al. 2009) and tilt meters and linear displacement sensors (ALMA, Rampini & Marchiori 2012),

in order to input real-time dynamic terms. The pointing model must be fit to "all-sky" pointing datasets, typically consisting of continuum scans on dozens of quasars scattered all about the sky, using fitting software such as TPOINT (Wallace 1994). When an antenna is relocated to a different pad, at least several terms of the pointing model must be remeasured and updated to counteract the small but inevitable changes in geometry. With the best pointing model in place, the so-called "blind pointing" performance refers to the typical pointing error after slewing to a particular direction. For the VLA, the blind pointing error is typically 10″ rms in calm nighttime conditions, but can exceed 60″ during the day. To improve the pointing accuracy during higher frequency observations, the technique of offset pointing is employed, in which local pointing corrections are periodically measured toward a bright quasar within $\sim 10^\circ$ of the science target. This technique can reduce the rms error to $\approx 3-5''$ for VLA antennas, and $\approx 1''$ for ALMA antennas (see Fig. 2.7).

2.7. Tracking errors and servo control system

In addition to static pointing error, antenna servo tracking errors are always present at some level and can cause time variation in the visibility amplitudes, particularly at high frequencies where the primary beam is smallest. At the VLA, the rms tracking error is about 3″ in low wind, which yields typical peak excursions of ±6″, or 10% of the primary beam at 43 GHz. While this sounds relatively harmless, it becomes critical when imaging extended objects. For example, at the phase center of a Gaussian beam, an rms tracking error of 10% of the beamwidth yields an amplitude variation of only 2.7%; however, at the half-power point of the beam, it yields a variation of ±28% (Figure 6). Tracking accuracy is generally the worst in high or gusty winds. In benign weather conditions, the tracking accuracy of an antenna is ultimately set by the quality of its servo control system. A description of a modern digital antenna servo control system for the 6 m diameter SMA antennas is given in Hunter et al. (2013). Good servo systems are designed with safety as the highest priority, with interlocking emergency-stop and hardware limit switches connected directly to the power source. Additional software safety measures include: 1) software motion limits, 2) consistency checks between the position feedback devices (encoders) and integrals of the velocity feedback devices (tachometers), 3) monitoring of motor currents and temperatures, 4) routine servicing of a watchdog timer which will trigger a system shutdown in case of a processing hangup, and 5) re-engaging of mechanical brakes whenever power is lost.

While all of the safety logic is running relentlessly in the background, the system must also compute the instantaneous torque to apply to track a celestial source at the sidereal rate, or perhaps perform faster on-the-fly imaging (Mangum et al. 2007). A typical servo design implements nested loops in which the calculations and adjustments operate at the appropriate rate. For example, the azimuth/elevation position loop runs at $\approx$ 10 Hz and computes velocity commands to send to the azimuth/elevation velocity loop running at $\approx$ 100 Hz, which in turn commands the motor current (torque) loop at $\approx$ 10 kHz. In the past, the gains of these loops (traditionally consisting of proportional, integral and derivative terms) were set in hardware by fixed values of resistors and capacitors. Similarly, the time constants of any filters on the feedback signals had to be set in this manner. In modern systems, these gains and filters are configurable in software, and can be adjusted (if necessary) when operating in different modes or under different conditions. Also, command-shaping can be implemented to smoothly transition between slewing and tracking modes to prevent overshoot and more rapidly

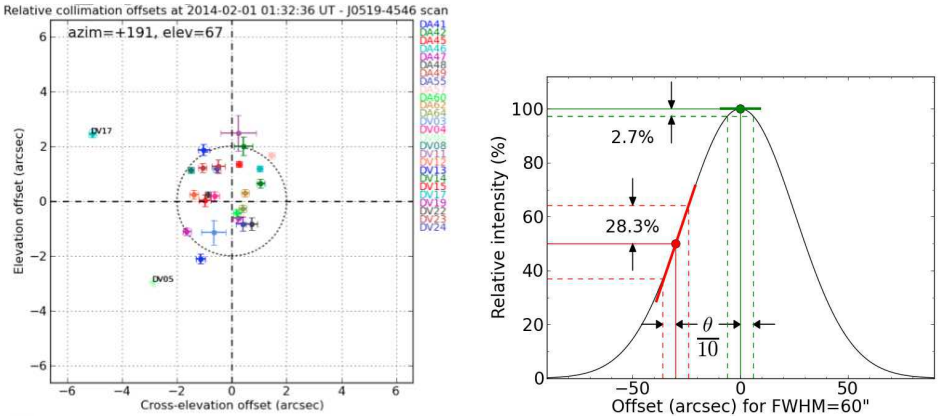

Figure 6. Left) Example of the blind pointing performance of ALMA in Band 3. The antenna offsets have been measured in an interferometric pointing scan and are mostly within the 2″ specification. Right) Comparison of the amplitude variation expected for a source at the center of a Gaussian beam vs. a source at the half-power point, in the face of only a modest tracking error (rms = 10% of the HPBW).

acquire the target (Hunter et al. 2013). Finally, more complicated algorithms can be attempted to try to achieve faster response times while avoiding the excitation of structural resonances (Gawronski 2008). Both the GBT (Whiteis & Mello 2012) and VLA (Jackson & Maglathlin 2011) are in the midst of an upgrade of their original servo system hardware and software.

3. Receivers

The role of the receivers in a synthesis telescope is to linearly amplify weak radio frequency signals while adding minimal noise, and down-convert them into room-temperature analog output signals on coaxial cables at intermediate frequencies (IFs) suitable for digitization. Receivers are traditionally comprised of a *front-end* (FE) and a *back-end* (BE). The FE includes the components that *must* be attached to the antenna, in contrast to the BE which includes the electronics (sometimes called the *IF chain*) that can be mounted in a separate rack and which process the IF signals. In this chapter, we will cover the FE polarization splitting device, the FE detector, and the BE electronics preceding the digitizers.

3.1. Overview of receiver technology

3.1.1. General configuration

Three current technological limitations can essentially explain the configuration of receivers in radio and (sub)millimeter astronomy. First, we can build broadband low-noise amplifiers (LNAs) with optimal noise performance up to about 120 GHz (see the review of Pospieszalski 2005). Second, we can digitize signals of instantaneous bandwidth up to about 2 GHz, which require a Nyquist sampling rate (Nyquist 1928)

of 4 gigasamples/second (Gs/s).[2] From these two facts, we can see that to observe at $\nu_{\rm RF} \gtrsim 120$ GHz, the first device in the front-end must be a device to downconvert the signal (called a mixer) instead of an amplifier. Also, to observe with an aggregate bandwidth > 2 GHz, a mixer must be present in the IF chain, regardless of the observing frequency. The third limitation is that when used as the first component in the front-end, both mixers and amplifiers must be cooled to cryogenic temperatures to yield competitive performance[3]. LNAs reach their optimal performance at about 15 K, which requires only a two-stage cryostat. In contrast, the best submillimeter mixers are superconducting tunnel junctions which require a more complicated three-stage cryostat to reach their optimal operating temperature of ≤ 4 K, a practical disadvantage compared to LNAs at $\nu_{\rm RF} \lesssim 120$ GHz. Putting together these facts, we can surmise that most ALMA FEs must begin with a cold mixer followed by a cold LNA, while VLA FEs begin with a cold LNA. Following these components, both ALMA and VLA receivers require room temperature mixers and amplifiers in their BEs, prior to digitization.

3.1.2. Polarization separation

For optimal sensitivity, we want to build dual-polarization receivers that can accept both polarizations from astronomical targets. This ability requires either dual linear or dual circular feeds. Because FE amplifiers and mixers operate on individual polarization signals, a polarization splitting device is needed. There are two broad categories of devices that can provide ∼ 20 dB of polarization purity with low loss: waveguide and quasioptical. The most common waveguide devices are called ortho-mode transducers (OMTs) and are placed between the feed horn and the FE device. An OMT is a four-port microwave device with three physical ports. It accepts a dual polarization signal into its one common input port (typically a square or circular waveguide) and splits the two polarizations into separate physical output ports (either rectangler waveguide or coax). OMTs can be designed numerically using software that solves Maxwell's equations. Although it can be challenging to achieve octave-wide (operating over factor of 2 in frequency) designs with good isolation and low loss (Skinner & James 1991), they are fairly straightforward to machine when the dimensions are large, i.e. at wavelengths longward of 1 mm (e.g. Asayama & Kamikura 2009; Kamikura et al. 2010), but good results have been obtained at 0.6 mm (ALMA Band 8; Naruse et al. 2009). The most common quasioptical splitter is a wire grid which reflects one polarization and transmits the other. Wire grids must be placed at a beam waist preceding the feedhorn, and the required wire separation is $\lesssim \lambda/20$ for good performance (Sørensen & Pontoppidan 2010; Houde et al. 2001; Chambers et al. 1988). At high frequencies, wire grids are easier to construct than OMTs. The disadvantage of wire grids is that you need two feedhorns (one per polarization) instead of one and each has an accompanying mirror to refocus the beam after the grid. Thus, optical alignment can be tricky and often leads to a significant *beam squint*, a condition in which the primary beams of the two polarizations differ in pointing direction by ∼0.1 beam (the ALMA specification) or worse.

---

[2] In fact, higher speed samplers are now being developed and fielded at submillimeter observatories (e.g. Patel et al. 2014), but 4 Gs/s was the limiting bandwidth when ALMA and EVLA were being designed.

[3] An exception to this rule is at low frequencies ($\nu_{\rm RF}$ <400 MHz) where the Galactic background increases from tens to thousands of Kelvin. In this regime, the room-temperature performance of LNAs is adequate without introducing extra noise.

3.2. VLA receivers

The VLA receiver system (Perley et al. 2009) consists of 10 bands (see Table 1 and Figure 7). The two lowest frequency bands employ crossed dipole feeds in front of the subreflector followed by room temperature amplifiers. The rest of the bands employ offset-Cassegrain corrugated feed horns followed by cryogenic LNAs housed in individual cryostats. The polarization splitters (Coutts 2011a,b) in between the feedhorns and the LNAs consist of quadruple-ridge OMTs ($\nu < 12$ GHz), waveguide (Bøifot junction) OMTs ($12 < \nu < 40$ GHz), or sloped septums (Q-band). At the input of the LNAs, most of the bands (those above 4 GHz) also employ isolators, which are passive, non-reciprocal two-port devices which, like a subway turnstile, prevent the propagation of signal in the reverse direction. In this case, the isolators serve to reduce leakage between the polarizations and reduce standing waves in the optics.

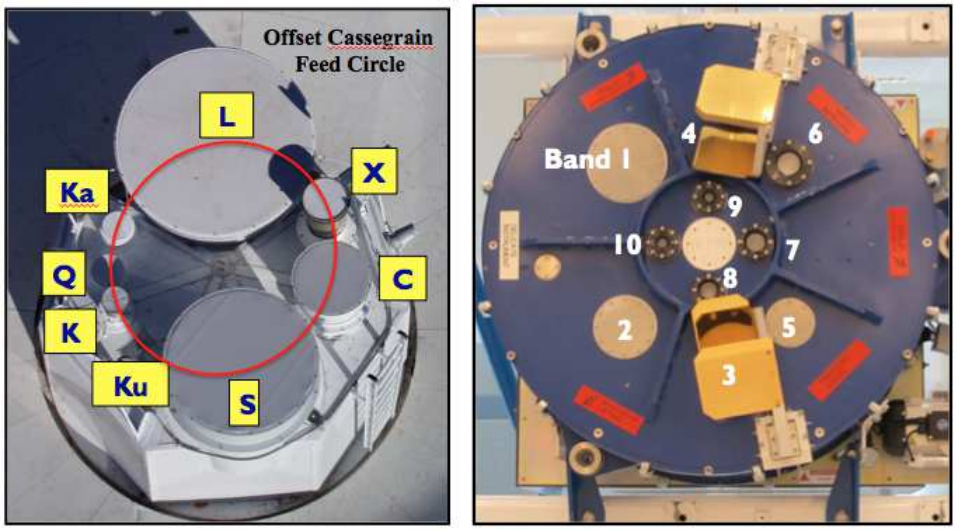

Figure 7. Left) Photograph of the VLA's offset Cassegrain feed circle, as viewed from the subreflector; Right) Top view of the ALMA cryostat with the vacuum windows labeled by band number (Table 1). The room temperature optics for Bands 3 and 4 are in place above their respective windows.

3.2.1. Amplifiers

An amplifier is an active, two-port device, meaning that it requires a voltage supply, and has one RF input and one RF output. The input signal emerges at the output with greater power (typically 10–30 dB, i.e. 10x–1000x) and is unchanged in frequency. The current generation of NRAO cryogenic LNAs on the VLA, VLBA, GBT, and other telescopes employ heterostructure field effect transistors (HFET) which operate at 15 K. They deliver a noise temperature performance of $\sim$ 4 K at low frequency and about 5 times the quantum noise limit at high frequency (ν>12 GHz, Pospieszalski 2012):

$$T_{\rm LNA}(\nu > 12{\rm GHz}) \approx 5h\nu/k = 10(\nu/42{\rm GHz})\ {\rm K}. \quad (5)$$

These indium-phosphide (InP) HFETs come from the "cryo3" series of wafers manufactured by Northrup Grumman Space Technology in 1999. At each frequency range,

Table 1. VLA and ALMA Receiver bands and their properties

Receiver band Central λ	code	Frequency range (GHz)	$\eta_{\rm Ruze}$[a]	Polarization type	splitter	Sideband type
VLA receivers						
4 m	4	0.058–0.084	1.0	dual linear	dipole	SSB
90 cm	P	0.23–0.47	1.0	dual linear	dipole	SSB
20 cm	L	1–2	1.0	dual circular	q.-r. OMT	SSB
13 cm	S	2–4	1.0	dual circular	q.-r. OMT	SSB
6 cm	C	4–8	0.99	dual circular	q.-r. OMT	SSB
3 cm	X	8–12	0.97	dual circular	q.-r. OMT	SSB
2 cm	K_u	12–18	0.94	dual circular	wg. OMT	SSB
1.3 cm	K	18–26.5	0.87	dual circular	wg. OMT	SSB
1 cm	K_a	26.5–40	0.74	dual circular	wg. OMT	SSB
7 mm	Q	40–50	0.57	dual circular	septum	SSB
ALMA receivers						
7 mm	1 (Q)	35–51[b]	1.0	dual linear	OMT[b]	SSB
4 mm	2 (E)	67–90[b]	1.0	dual linear	OMT[b]	SSB
3 mm	3 (W)	84–116	0.99	dual linear	OMT	2SB
2 mm	4	125–163	0.99	dual linear	OMT	2SB
–	WVR	175.3–191.3	0.98	single linear	–	DSB
1.6 mm	5	163–211	0.98	dual linear	OMT	2SB
1.3 mm	6	211–275	0.96	dual linear	OMT	2SB
0.9 mm	7	275–373	0.93	dual linear	wire grid	2SB
0.7 mm	8	373–500	0.87	dual linear	OMT	2SB
0.45 mm	9	600–720	0.74	dual linear	wire grid	DSB
0.35 mm	10	787–950	0.59	dual linear	wire grid	DSB

[a]Assuming $\sigma = 400\mu$m for VLA and $\sigma = 20\mu$m for ALMA
[b]Bands under development
References for ALMA bands: 1: Huang et al. (2016); 3: Kerr et al. (2014); Claude et al. (2014); 4: Asayama et al. (2008); 5: Billade et al. (2012); 6: Kerr et al. (2014); 7: Mahieu et al. (2012); 8: Sekimoto et al. (2008); 9: Baryshev et al. (2015); 10: Gonzalez et al. (2014); Fujii et al. (2013); Uzawa et al. (2013), WVR: Emrich et al. (2009)

there exists an optimal size (gate periphery) for a transistor that facilitates the design of a broadband amplifier. The gate peripheries range from 200 μm at Ku-band (and below) down to 30 μm at W-band. The HFET devices are housed inside a block of gold-plated brass and the input is connected by either coaxial cable (low frequency receivers) or waveguide (high frequency receivers) to the corresponding OMT output. The LNA package has a total gain of $\approx$ 35 dB. To avoid feedback, the HFETs are mounted in a channel small enough to block all waveguide modes in the band of operation. Electrical connections are made via microstrip and bond wires. It is important to note that the LNA is not the only contributor to the overall receiver temperature ($T_{\rm rx}$). While the details and measurements can be found in the EVLA memo series, a rough model for the mid-band $T_{\rm rx}$ for VLA bands above 12 GHz is $T_{\rm rx} \approx 2 + 0.5\nu_{\rm GHz}$ K.

3.2.2. Mixers

Mixers were invented around the time of World War I for radio direction finding (see the historical review of Maas 2013). A mixer is a three-port device which accepts two inputs: a broad RF signal and a narrow LO continuous wave (CW) tone, and produces a broadband IF output signal. This frequency conversion occurs in a diode with a strongly nonlinear current (I)-voltage (V) characteristic, $I = f(V)$. As an example, consider a simple square-law diode for which

$$I = \alpha V^2. \tag{6}$$

When the two input fields are superposed:

$$V = V_{\rm RF}\cos(\omega_{\rm RF}t) + V_{\rm LO}\cos(\omega_{\rm LO}t) \tag{7}$$

the non-linear nature of the mixer will effectively multiply the LO and RF signals together. This effect can be seen by substituting equation Eq. 7 into Eq. 6, which produces three terms for the resulting current, including the cross term which can be expanded by a trigonometric identity into:

$$2V_{\rm RF}V_{\rm LO}\cos(\omega_{\rm RF}t)\cos(\omega_{\rm LO}t) = V_{\rm RF}V_{\rm LO}[\cos(\omega_{\rm RF}-\omega_{\rm LO})t + \cos(\omega_{\rm RF}+\omega_{\rm LO})t]. \tag{8}$$

Thus, current will flow at the difference frequency of the LO and IF. It is important to notice that the multiplication serves to transfer the phase from the RF signal to the IF signal, a process called heterodyning. Because they can transfer phase in this manner, mixers are key components for interferometers.

Mixers range from low-cost, off-the-shelf packages using Si Schottky diodes that operate at room temperature (in cell phones etc.) to the expensive, delicate, research-grade Superconductor-Insulator-Superconductor (SIS) tunnel junctions that were developed in the late 1970s (Dolan, Phillips & Woody 1979; Richards et al. 1979; Rudner & Claeson 1979) and early 1980s (Pan et al. 1983; Wengler et al. 1985) and today serve as the cryogenic FE detector for ALMA Bands 3 through 10. At terahertz frequencies, the performance of SIS mixers declines and hot-electron bolometer mixers are used instead (e.g. Meledin et al. 2004). Room temperature mixers are also employed in ALMA and VLA IF circuitry after the received signal has been sufficiently amplified so that their conversion loss is of little consequence. Typically, the IF signal output by a mixer will contain overlapping signals from two frequency ranges termed *sidebands* (see Figure 8), resulting in double sideband (DSB) performance. One sideband represents a

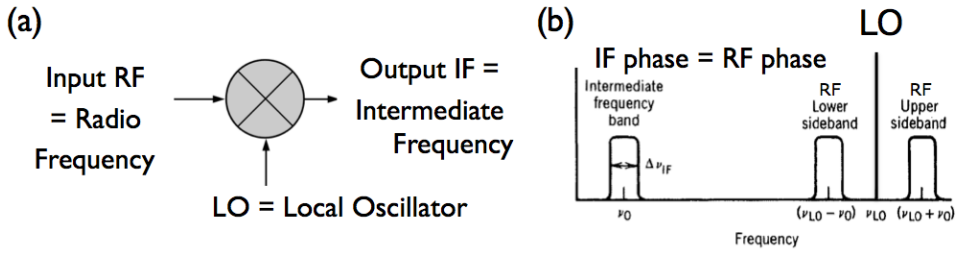

Figure 8. a) Schematic representation of a mixer's input and output signals; b) Spectrum showing the relative frequencies and bandwidths of the signals.

piece of the RF spectrum above the LO frequency and the other is a piece below the LO frequency. The DSB confusion can be avoided either by pre-filtering the RF signal (termed an SSB mixer), or by designing a mixer to separate the sidebands into separate IF outputs (termed a 2SB mixer). If only one of the sidebands from a 2SB mixer is desired, the IF output corresponding to the unwanted sideband can be terminated into a load (such as a waveguide absorber), which is a configuration termed a 1SB mixer [4]. VLA receivers employ SSB mixers, as is likely for ALMA bands 1 and 2 (still under development). ALMA bands 3 through 8 are 2SB, while bands 9 and 10 are DSB, as are all receivers on the SMA (Blundell 2004). The relative sensitivities of these mixer types has been evaluated for the ALMA site (Iguchi 2005; Jewell & Mangum 1997), but in general 2SB is superior to DSB. A development project to upgrade the band 9 mixers into 2SB format is underway (Khudchenko et al. 2012).

3.3. ALMA receivers

The ALMA receiver system consists of ten frequency bands (Table 1), all housed in the same 0.97 m diameter, 450 kg cryostat (Figure 7) which is mounted inside the receiver cabin at the Cassegrain focus. Currently, a receiver band is brought into focus by adjusting only the pointing of the primary mirror to orient the desired sky direction toward the desired receiver window. There is some improvement to be gained from also adjusting the subreflector to tilt approximately half-way toward the selected receiver (Hills 2005), but this added complication has not yet been introduced into the system since the pointing and focus models will need to account for it. A low-loss polymer membrane, initially made of Gore-Tex (Candotti et al. 2006; Koller et al. 2006) but replaced by Teflon fluorinated ethylene propylene (FEP), protects the cabin from the outdoor environment. The ALMA FE optics have three generic layouts (Rudolf et al. 2007). Bands 1 and 2 use room-temperature (external to the cryostat) polymer lenses as the focusing element. Bands 3 and 4 are in the outermost position in the cryostat and use a pair of external room-temperature mirrors (Band 3 includes a Teflon lens on the corrugated feedhorn, Claude et al. 2008). The focusing optics for the higher bands are off-axis ellipsoidal mirrors mounted on the cold cartridge assemblies (CCAs) inside the cryostat. The diameters of the cryostat windows are set large enough to avoid significant truncation losses (Lamb 2003). For polarization separation, ALMA bands 7, 9 and 10 use wire grids while the other bands use OMTs (Table 1). The SIS mixers and their enclosing CCAs in the ALMA receivers were constructed by different international parties (see the references in Table 1). In all cases, the receiver noise performance meets specification, beginning with 41 K in Band 3, and essentially following the function $4h\nu/k$ in the higher bands. Finally, the room-temperature Dicke-switched water vapor radiometer (WVR) in each antenna has proven effective and essential to removing atmospheric phase fluctuations on short timescales, down to the adopted integration time of 1.152 second (6×0.192), and on all baseline lengths (Nikolic et al. 2013).

3.4. Local oscillators (LOs)

Being required to drive mixers (§ 3.2.2), an LO signal must be a clean tone with high signal to noise ratio (SNR) in order to obtain accurate astronomical spectra. LOs are

[4] Another way to achieve a 1SB mixer is to terminate the unwanted RF sideband of a 2SB mixer into a cold load ahead of the mixer using a Martin-Puplett diplexer (Martin & Puplett 1970; Lesurf 1988).

constructed from a base oscillator with a high-Q electro-mechanical feature, such as a tunable cavity or a resonant sphere, which is ultimately synchronized to an atomic frequency standard. For ALMA, the fundamental oscillators located in each warm cartridge assembly (WCA) are commercially-produced yttrium iron garnet (YIG) spheres embedded in a magnetic field generated by the sum of a coarse tuning coil and a fine tuning (FM) coil. These compact YIG packages produce clean tones in the 2-40 GHz range and are also used in the VLA. For the higher frequency bands of ALMA, the YIG tone must be multiplied by one or more integer multiplication stages, many of which include power amplifiers to boost the multiplied signal. All of the LOs for ALMA (Bryerton et al. 2013) and VLA were built by NRAO. The LO supplying the first mixer in the FE is often called LO1 in order to distinguish it from the LOs in the BE, which are numbered starting from LO2.

3.4.1. Phase-lock loops (PLLs)

Although a free-running YIG tone is typically very clean, it is subject to drift in frequency with time, and its close-in phase noise (i.e. the line-broadening of the tone) is not negligible. In contrast, a radio telescope requires a precisely stable LO frequency in order to observe spectral line features. An interferometer has a further requirement that the receivers in all antennas be phase-locked so that celestial signals will correlate. A circuit to stabilize and lock the LO is called a phase-lock loop (PLL). A good description of a modern digital PLL used on the SMA interferometer is given in Hunter et al. (2011b). Similar in concept to an antenna servo (§ 2.7), the PLL circuit continuously analyzes the phase difference with respect to an accurate low-frequency reference signal (of order 20–100 MHz), which is produced by a device called the First LO Offset Generator (FLOOG) in NRAO terminology. The PLL computes and applies a correction to the FM tuning magnetic coil of the YIG in order to maintain lock. The bandwidth of the correction circuit is typically a 0.5-1 MHz, which enables rapid re-locking after a Walsh cycle phase change (see § 3.4.2). Initial lock is achieved by starting from a computed (or a look-up table) tuning value and sweeping the coarse coil until the tone is at the prescribed location in the IF of the PLL (see, e.g. Garcia & Alvarez Barros 2012). A PLL typically relies on an external mixer to downconvert the signal from the LO being controlled to a value close to the frequency of the low-frequency reference, and this external mixer in turn relies on an accurate high-frequency reference signal for its LO. For ALMA, this reference signal is delivered by a photomixer (Huggard et al. 2002) located in each WCA which converts the photonic frequency reference distributed via fiber optic cable and originating from the laser synthesizer (Ayotte et al. 2010) in the Central LO (Shillue et al. 2012). In fact, the fundamental references for LO2 in the BE and for the FLOOG in the WCA are also distributed on the same fiber using wavelength division multiplexing.

3.4.2. LO modulation

In an interferometer, aside from enabling the mixers to operate, the LOs are also crucial for implementing many additional features that ensure data quality (Thompson et al. 2007). Very fine control of the frequency and phase of LO1 is inserted via the PLL reference generated by a direct digital synthesizer (DDS), which is part of the FLOOG in NRAO systems. For example, suppression of spurious tones and DC offset is achieved by modulating LO1 with 180° phase switching using a Walsh function sequence (Granlund et al. 1978; Emerson 2008) and removing it after digitization by ad-

justing the digital signal datastream in a supplementary fashion (i.e. via a sign change). This technique serves to wash out any signals in the digital datastream that did not enter at the FE mixer (i.e. those that did not originate from the sky). In high spectral resolution modes, 180° phase switching does not work well (Napier 2007), so a complementary technique is used by ALMA called LO offsetting (Kamazaki et al. 2012). In this case, each antenna's LO1 is shifted by a different small amount (in integer steps of 30.5 kHz = 15625/512), then this shift is removed downstream in LO2 or a combination of LO2 and the tunable filter bank (TFB) LO (sometimes called LO4) in the baseline correlator. In the VLA, the LO offsetting technique is called "f-shift" and uses prime number frequency steps, which are removed by the fringe rotators in the Wideband Interferometer Digital Architecture (WIDAR) correlator (Carlson & Dewdney 2003). A spurious signal that enters the system between the insertion and removal points receives a residual fringe frequency equal to the spacing of the shifts between antennas and is suppressed upon normal integration of the data. In particular, LO offsetting can supply more than 20 dB of additional rejection of the unwanted image sideband in 2SB receivers. This extra suppression is crucial to eliminate strong spectral lines whose remnants may otherwise survive the moderate (10-20 dB) suppression supplied by a 2SB receiver alone. In practice on ALMA, LO offsetting also reduces residual closure errors. Finally, the two sidebands in a DSB receiver (§ 3.2.2) can be quite effectively separated ($\geq$ 20 dB) by applying 90° Walsh phase switching. In this manner, both sidebands can be recovered simultaneously in the correlator, thus doubling the effective bandwidth, as is done on the SMA (Patel et al. 2014). However, Walsh switching will not remove image signals which are not common to all antennas, including the atmospheric noise from the image sideband in a DSB receiver.

3.5. Back-end components

3.5.1. Round trip phase (RTP) measurement and correction

The required distribution of the LO reference signals in large arrays like ALMA and VLA occurs via many kilometers of fiber optic cables. Optical fibers offer many advantages to radio interferometers, including low loss and wide bandwidths (Young 1991). However, the thermal expansion coefficient of these fibers combined with the diurnal temperature change of the environment leads to temporal changes in the optical path length of the fiber that vary as a function of antenna pad location. Although the cables are buried, the thermal effect is still significant and causes delay changes to the LO references carried by the fiber[5]. Mechanical stresses on the above-ground portions of the fiber are also significant (D'Addario & Stennes 1998). To compensate for these problems, ALMA employs a line length correction (LLC) system, which uses a piezoelectric fiber stretcher driven by a PLL to maintain a constant optical path length on each fiber during an observation (Shillue et al. 2012). In principle, the stretcher requires only enough range to compensate drift between visits to the phase calibrator, provided that the stretchers are only ever reset to the center of their range in between consecutive integrations on the phase calibrator *and* that the offline calibration software (CASA) is aware of the resets. In practice, this synchronization has not been implemented in the ALMA system (nor in CASA), mainly because the stretchers have been found to have

[5]The SMA uses custom-designed low thermal coefficient optical fiber that is no longer commercially produced. Over the modest fiber lengths (500m or less), it obviates the need for an RTP system.

sufficient range to handle drifts over a few hours (even on 10 km baselines) before slipping a fringe, which is longer than current (Cycle 3) standard ALMA observing blocks (< 90 minutes).

The EVLA project also built a round trip phase (RTP) measuring system to mitigate project risk when it was not clear what the stability performance of the fiber would be (Morris et al. 2008; Durand & Cotter 2002). The RTP was designed to be able to measure and send corrections to the EVLA WIDAR correlator. Although the VLA has longer baselines, it operates at lower frequencies, and the amount of phase change in the fiber observed by the RTP was small and slow compared to atmospheric phase variations (and thus are effectively removed by the normal phase calibration sequence). However, the RTP was very useful in diagnosing phase vs. elevation changes due to antenna electronics and temperature changes *not* in the fiber, thus allowing those problems to be identified and fixed. Although the RTP system was deactivated in 2010, it can be re-activated if needed, e.g. for a future Pie Town link.

Although it is not implemented as a round-trip measurement, the VLBA has a pulse-cal system to measure the relative instrumental phase between baseband channels (Walker 1995; D'Addario 1996). A train of 1 MHz or 5 MHz pulses from a tunnel-diode are injected into a directional coupler, the same one used to inject the signal from the $T_{\rm cal}$ noise diode (see § 3.6.2). The pulses pass through the LNA and all downstream processing and the resulting phases are detected for selectable tones in the back-end. These so-called $P_{\rm cal}$ data are supplied to the user and can be used to calibrate the phase characteristics (offset and frequency slope) of the antenna's components independent of the atmosphere or whether a calibrator is being observed.

3.5.2. Square law detectors and IF level setting

Two unglamorous but essential parts of the receiver BE are the ability to: 1) measure the total power of signals using square law detectors (SQLDs) which convert the power in a continuum signal into voltage (Bare et al. 1965); and 2) adjust signal levels in order to optimize the inputs into successive devices along the IF chain. For example, when the input signal to an amplifier exceeds its specified input range, it no longer functions in a linear fashion. In other words, the effective gain factor is less than what it would be with a smaller input. This effect is termed "gain compression", and is often accompanied by other bad characteristics including spurious oscillations and change in the bandpass shape. To avoid these pitfalls, all observations begin with the insertion of a known load (possibly just blank sky) into the beam followed by a sequential adjustment of the programmable attenuators placed strategically along the IF chain in order to achieve optimal levels, which are implemented as target values at each set of SQLDs. An attenuator is a wideband two-port device that dissipates a fraction of the input power into a resistor. Programmable attenuators typically have a range of 0-15 or 0-31 dB with steps of 0.5 or 1 dB.

After the final mixing stage, the signal to be digitized has reached its lowest frequency, which is traditionally termed a *baseband* even if the low end of the band is not at 0 Hz. In ALMA and VLA, each of the 2 GHz-wide basebands covers 2-4 GHz. After passing through an analog anti-aliasing filter (Holmes & Brundage 2008), the ALMA baseband signals are sampled in the second Nyquist zone of the 3-bit 4 Gs/s sampler (Deschans et al. 2002). Adjusting the power level in each baseband is also essential as it represents the input level to the digitizers, which often have a narrow range of input power over which the SNR is optimal, and is particularly true for ALMA. In fact,

ALMA observations must set and remember two different sets of attenuation levels – one set used for the system temperature scans (to avoid saturation on the hot load) and one set used for normal observing. The VLA includes an additional device called a gain slope equalizer, which allows the signal power to be adjusted in a frequency-dependent manner providing a more uniform level across the baseband fed to the digitizers (Morgan et al. 2007). The ALMA Band 10 receiver also includes an equalizer in the IF section of its WCA (Fujii et al. 2013). Finally, SQLDs can also be used independently of the autocorrelation portion of the correlator to perform continuum pointing or focus scans, and to measure the baseband-averaged system temperature T_{sys}.

3.6. Measurement of system gain and sensitivity during observations

3.6.1. T_{rx} and T_{sys} measurement at ALMA

In all ALMA observations, the T_{rx} and T_{sys} in each baseband is measured periodically to be able to properly calibrate the data and account for atmospheric absorption. By design, the measurement is a spectral measurement in order to capture the inherent variation of the receiver sensitivity across the observing band, and to capture the spectral variation in atmospheric opacity due to molecular absorption features (Paine & Blundell 2004, e.g.). The measurement is achieved using three autocorrelation spectra measured sequentially on: the sky, the ambient temperature load, and the heated load. The loads are temperature-controlled blackbodies with nearly perfect emissivity (0.999, Murk et al. 2010) mounted in the mechanically-driven ALMA Calibration Device (Figure 9). The online software (TelCal, Broguière et al. 2011) takes the two load spectra to compute T_{rx} via the y-factor method (see Eq. 12 in the chapter on Basics of Radio Astronomy). TelCal then uses this result along with the sky spectrum and the atmospheric model (Pardo et al. 2001) to compute T_{sys} using the chopper wheel method (e.g. Jewell 2002). It accounts for the relative sideband gain, currently using a single value per baseband, but it could eventually be a spectrum. These temperature spectra are stored in the data and applied offline in CASA to place the visibilities onto an absolute temperature scale and to set the relative weights of the data. An example of the three measurements and the resulting T_{rx} and T_{sys} spectra are shown in Figure 10. Although the power level varies by a factor of three across the baseband, the overall receiver sensitivity is fairly constant. However, the fact that the T_{sys} spectra show upward spikes at the frequencies of atmospheric molecular absorption lines (in this case from ozone) reflects the fact that those channels are less sensitive in the data, and hence can be down-weighted (using the spectral weights option available in CASA version $\geq$ 4.3). This capability is important to obtain the best performance when combining all the channels of all the spectral windows to obtain a single multi-frequency synthesis (mfs) continuum image. Currently, all T_{sys} spectra are obtained in the low resolution mode of the baseline correlator, time division mode (TDM), which yields 15.625 MHz channels in dual-polarization mode (Escoffier et al. 2007). For higher resolution spectral windows obtained in frequency division mode (FDM), the T_{sys} correction must be interpolated to narrower channels when applied to the data in CASA. A future software upgrade should allow T_{sys} spectra to be obtained directly in FDM spectral windows, which will provide an additional benefit of improved removal of atmospheric lines. This capability was introduced on the ACA correlator starting in ALMA Cycle 3.

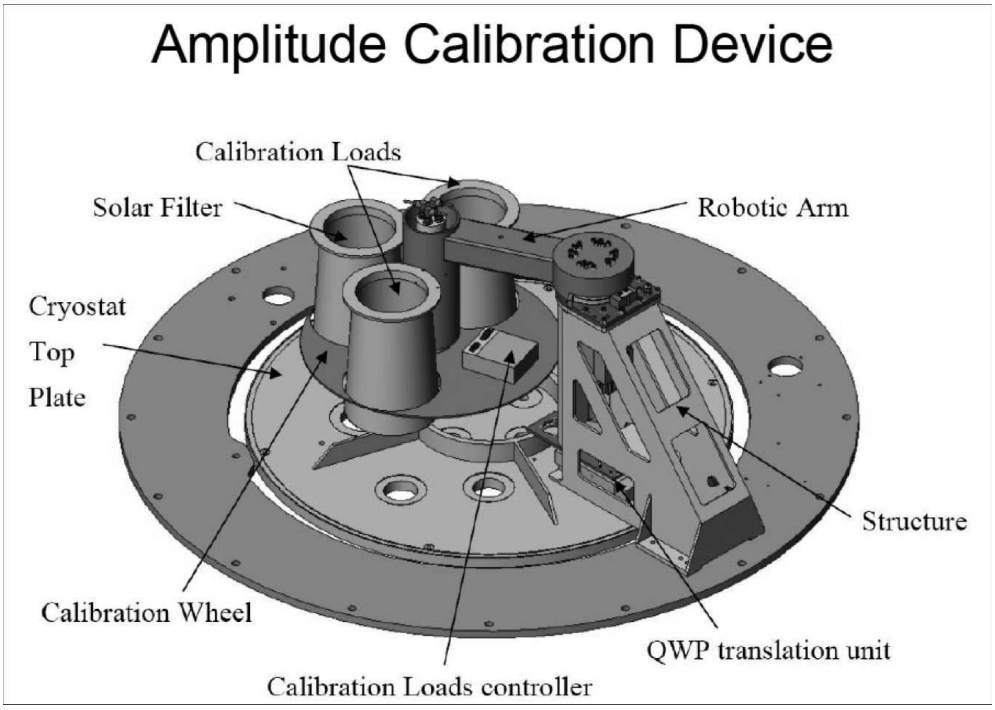

Figure 9. Diagram of the ALMA Calibration Device located between the cryostat and the membrane, and mounted on the Front End Support Structure (the outer ring in the diagram). The quarter wave plate (QWP) unit was designed to convert the Band 7 linear feeds to circulator polarization, but it is not currently populated.

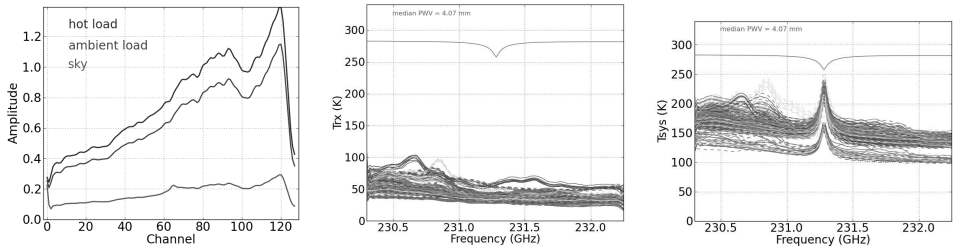

Figure 10. Left panel) An overlay of three successive ALMA observed spectra in Band 6 from one 2 GHz-wide baseband acquired: on the sky, on the ambient load and on hot load; Middle panel) The T_{rx} spectra from all antennas and both polarizations overlaid on one another; Right panel) The corresponding T_{sys} spectra overlaid on the same vertical scale as the T_{rx}. The upper curve in the latter two panels is the atmospheric transmission spectrum, showing the presence of an ozone (O_3) line ($16_{1,15} - 16_{0,16}$), which causes an increase in the T_{sys} in those channels.

3.6.2. T_{cal} and T'_{sys} measurement at VLA

An alternative to a mechanized load system is a broadband calibrated noise diode that is switched on and off at a high rate ($\approx$ 20 Hz). At the expense of a slight increase in system noise, it provides a stable modulated reference signal. Each VLA receiver contains such a diode with a noise temperature (T_{cal}) measured in the laboratory on

a 25-100 MHz grid (depending on the band). A synchronous detector located in the WIDAR station boards calculates the sum ($P_{\rm on}+P_{\rm off}$) and difference ($P_{\rm on}-P_{\rm off}$) powers along with the ratio R and $T'_{\rm sys}$ every second:

$$R = \frac{2(P_{\rm on} - P_{\rm off})}{P_{\rm on} + P_{\rm off}} \text{ and } T'_{\rm sys} = \frac{T_{\rm cal}}{R}. \quad (9)$$

These values are stored in the switched power table of the astronomical data. Application of $T'_{\rm sys}$ in AIPS or CASA places the visibilities on an absolute temperature scale. It also removes any gain variations in the electronics between the diode and the correlator down to 1 second timescales. Only a single $T'_{\rm sys}$ value per subband is computed, using an interpolated value from the $T_{\rm cal}$ grid; thus, the spectral resolution of the correction is typically coarser than ALMA's channelized $T_{\rm sys}$. Also, in contrast to the $T_{\rm sys}$ discussed in § 3.6.1, the definition of $T'_{\rm sys}$ is with respect to the receiver input, so it does not account for the effect of the atmosphere. The resulting elevation-dependence of the gain can be compensated for in the offline software using a measurement or estimate of the zenith opacity. It is worth noting that WIDAR's digital requantization of the 3-bit or 8-bit signal into a 4-bit signal introduces an additional gain change after the synchronous detector. This gain change is automatically applied to the 3-bit data online and is also stored in the same table for reference.

4. Derivation and simulation of the radiometer equation

The radiometer equation is fundamental to radio astronomy as it predicts the expected standard deviation of repeated measurements of the antenna noise temperature based on finite time samples. It is based on a few concepts in physics and statistics which can be easily simulated on a computer. Here we present a simulation which illustrates the fundamental derivation of this equation. The derivation can be found in more detail in Hunter et al. (2015). Shown in Figure 11 is the time series and corresponding histogram of a wide-sense stationary random RF signal (often termed "white noise"), whose amplitude (x_n) follows Gaussian statistics and has a mean value of zero and a variance σ^2 equal to the mean power P (Shannon 1949). We have set the mean power to 4 in arbitrary units. Shown in Figure 12 is the square of the amplitude which is the instantaneous noise power, and its histogram, which follows the expected gamma distribution. For any chosen sample of the noise power, statistics tells us that the standard error of the mean will have a distribution variance of $\sigma_{\rm P}^2 = 2\sigma^4/N$ where N is the number of samples (Fisher 1930). The number of statistically independent samples in time τ of a signal with bandwidth (β) is $N = 2\beta\tau$ (Oliver 1965). Thus, the expected standard deviation of the power is $\sigma_{\rm P} = \sigma^2/\sqrt{\beta\tau}$. In the limit of large N, the mean of the gamma distribution is the expectation mean of x_n^2 and is equivalent to P, thereby yielding the traditional radiometer equation:

$$\sigma_{\rm P} = \frac{P}{\sqrt{\beta\tau}}. \quad (10)$$

Since $P \propto T$ in the Rayleigh-Jean limit (Johnson 1928), it can also be written in terms of $\sigma_{\rm T}$, with $T_{\rm sys}$ in place of P (as is done in Eq. 14 of the chapter on Basics of Radio Astronomy; see also Randa et al. 2008).

In Figure 13, we simulate observing the RF signal with a single-dish telescope for increasing values of the sample size N. In the left panel, we break the datastream of

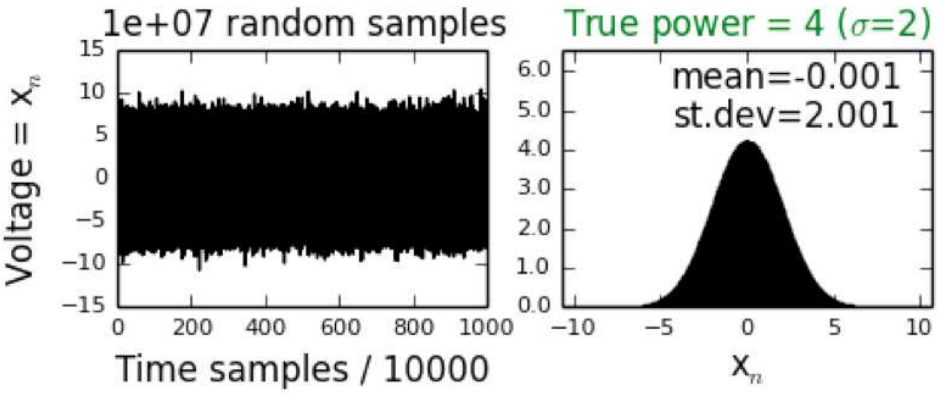

Figure 11. Simulated time series with 10^7 random samples of a white noise RF signal. Left panel) voltage vs. time. Right panel) the corresponding histogram of the voltage, for which the computed mean and standard deviations are listed.

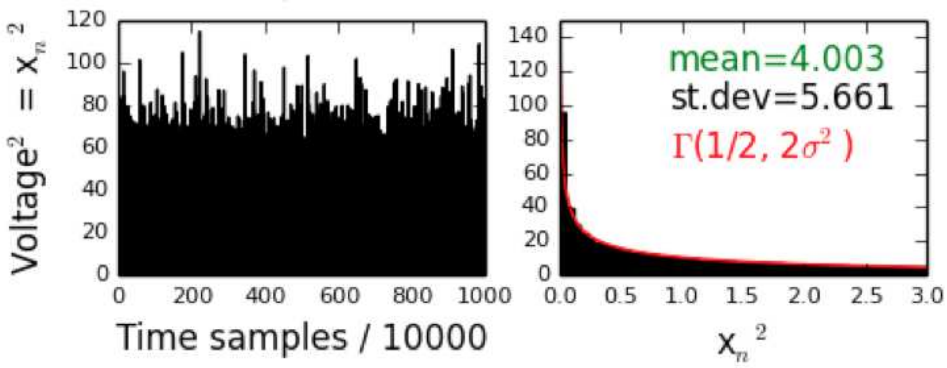

Figure 12. Left panel) The power vs. time of the signal in Figure 11. Right panel) the corresponding histogram of the power, for which the computed mean and standard deviations are listed. The envelope of the histogram is a gamma distribution with parameters of 1/2 and 8.

10^7 samples into 10^5 observations each containing $N = 100$ samples. Each observation provides an estimate of the noise power and is placed into the corresponding bin of the histogram. The distribution peaks near the value of 4.0 but with a broad uncertainty of $\sigma_P = 0.564$, yielding an SNR of 7.07. The expected uncertainty of the variance, $\sqrt{2\sigma^4/N}$, is 0.566. Thus, the prediction of the radiometer equation matches the simulated result to < 0.4%. In the second panel, we increase the size of each observation to 1000 samples, and place each of the resulting 10^4 noise power estimates into the corresponding power bin. The peak of the distribution remains close to 4 while the width of the distribution becomes narrower. The uncertainty is now ±0.180 and the SNR is now 22.6. In this case, the radiometer equation predicts an uncertainty of ±0.179. Finally, in the third panel, the size of each observation is increased to 10000 samples. The resulting uncertainty in the noise power is now down to ±0.057, again matching the prediction of the radiometer equation. The SNR is now 70.2. To summarize, we

have increased the observation time τ by a factor of 100 and the SNR has improved by a factor of 10.

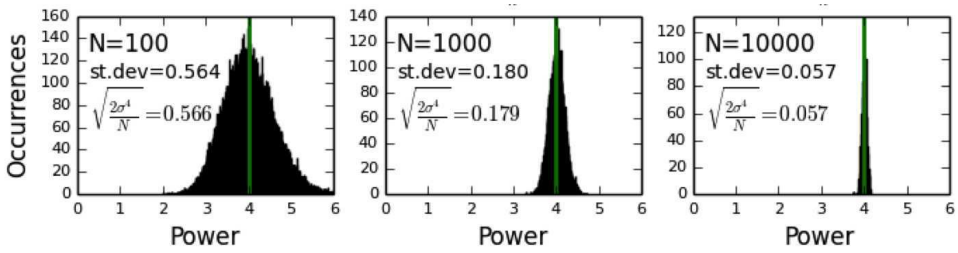

Figure 13. The three panels show the results of a computer simulation of the radiometer equation, in which 10^7 random samples of an RF signal with power = 4 are successively "observed" with three different observation lengths containing N=100, 1000, and 10000 samples. The uncertainty of the measured power (i.e. its standard deviation) is visualized by the width of the histogram, which decreases with $1/\sqrt{N}$.

The radiometer equation applies equally well to an interferometer. However, because cross-correlation represents a multiplication of two independent, zero-mean RF signals (in contrast to auto-correlation which effectively squares a single signal), the resulting product is not positive definite like it is in Figures 12 and 13. Instead, the mean of the distribution gives the correlated power rather than the total power. Thus, it can be zero if there is no source in the beam, although the variance will not be zero. A similar numerical simulation shows that the uncertainty of the variance of this cross-correlation product is: $\sigma_P = \sqrt{\sigma^4/N}$. Thus, the noise on any given baseline is lower than the single-dish case by is $\sqrt{2}$, which is consistent with the general formula that the SNR scales as $1/\sqrt{\text{number of baselines}}$ (e.g. Wrobel & Walker 1999). This result implicitly assumes that the antennas have equal collecting area and efficiency, and that we are in the limit that the correlated signal is small compared to the noise. Of course, the cross-correlation data product is more commonly examined in terms of amplitude and phase rather than power. The expected probability distributions of these component quantities as a function of the SNR are given in Crane & Napier (1989).

We conclude with a note of caution. All receivers (SIS mixers and LNAs) exhibit gain fluctuation at some level (e.g. HEMTs, Gallego et al. 2004; Wollack 1995), which can lead to a performance that is worse than predicted by the radiometer equation if the statistics of the noise is non-stationary. Non-stationary noise typically exhibits a power law spectrum, i.e. noise $\propto f^{-\alpha}$, and its variance diverges with time (Hunter et al. 2015). Another source of gain fluctuation is cryostat temperature fluctuations that reach the cold mixer (Kooi et al. 2000), which can be compensated by adjusting the voltage bias of the subsequent LNA in real time (Battat et al. 2005). Regardless of the origin of the instability, the receiver total power output stability vs. integration time is often characterized by the Allan variance (see D'Addario 2003, and references therein). At short integrations, the sensitivity follows the expected curve for white noise but eventually levels off and will begin to increase at longer integrations. Thus, in general, the integration time must be kept short to avoid losing sensitivity.

Acknowledgments. The National Radio Astronomy Observatory is a facility of the National Science Foundation operated under agreement by the Associated Universities, Inc. ALMA is a partnership of ESO (representing its member states), NSF

(USA) and NINS (Japan), together with NRC (Canada) and NSC and ASIAA (Taiwan) and KASI (Republic of Korea), in cooperation with the Republic of Chile. The Joint ALMA Observatory is operated by ESO, AUI/NRAO and NAOJ. This research made use of NASA's Astrophysics Data System Bibliographic Services and the SPIE and IEEE Xplore digital libraries. The authors thank Vivek Dhawan, Anthony R. Kerr, and Marian W. Pospieszalski of NRAO for comments, corrections and improvements, and Robert Kimberk of the Harvard-Smithsonian Center for Astrophysics for discussions and research on the radiometer equation.

References

Ananthakrishnan, S. 1995, Journal of Astrophysics and Astronomy Supplement, 16, 427
Asayama, S., Kawashima, S., Iwashita, H., et al. 2008, 19th International Symposium Space Terahertz Technology, 244
Asayama, S., & Kamikura, M. 2009, Journal of Infrared, Millimeter, and Terahertz Waves, Volume 30, Issue 6, 573
Ayotte, S., Babin, A., Poulin, P., et al. 2010, International Topical Meeting on Microwave Photonics, 2010, p. 249-252, 249
Baars, J. W. M. 2007, Astrophysics and Space Science Library, 348
Baars, J. W. M., Lucas, R., Mangum, J. G., & Lopez-Perez, J. A. 2007, IEEE Antennas and Propagation Magazine, 49, 24
Baars, J. W. M., Martin, R. N., Mangum, J. G., McMullin, J. P., et al. & Peters, W. L. 1999, PASP, 111, 627
Baars, J. W. M., & Hooghoudt, B. G. 1974, A&A, 31, 323
Bare, C. C., Steppe, A., & Thacker, D. 1965, IEEE Proceedings, 53, 2155
Baryshev, A. M., Hesper, R., Mena, F. P., et al. 2015, A&A, 577, A129
Battat, J., Blundell, R., Hunter, T. R., et al. 2005, IEEE Transactions on Microwave Theory & Techniques, 53, 389, arXiv: 0710.0694
Bennett, J. C., Anderson, A. P., McInnes, P. A., & Whitaker, A. J. T. 1976, IEEE Transactions on Antennas & Propagation, 24, 295
Bhatnagar, S., Cornwell, T. J., Golap, K., & Uson, J. M. 2008, A&A, 487, 419
Billade, B., Nystrom, O., Meledin, D., et al. 2012, IEEE Transactions on Terahertz Science & Technology, 2, 208
Blundell, R. 2004, 15th International Symposium on Space Terahertz Technology, 3, arXiv: astro-ph/0508492
Boothroyd, A. I., Blagrave, K., Lockman, F. J., et al. 2011, A&A, 536, AA81
Bosma, M. B. 1998, SPIE Proceedings, 3357, 646
Broguière, D., Lucas, R., Pardo, J., & Roche, J.-C. 2011, Astronomical Data Analysis Software and Systems XX, 442, 277
Bryerton, E., Saini, K., Muehlberg, J., Vaselaar, D., & Thacker, D. 2013, IEEE MTT-S International Microwave Symposium Digest, 6697622
Butler, B. J. 2003, ALMA Memo 479, https://library.nrao.edu/public/memos/alma/memo479.pdf
Carlson, B. R., & Dewdney, P. E. 2003, New technologies in VLBI, ASP Conference 306, 271
Candotti, M., Baryshev, A. M., Trappe, N. A., et al. 2006, 17th International Symposium on Space Terahertz Technology, 280
Chambers, W. G., Costley, A. E., & Parker, T. J. 1988, International Journal of Infrared and Millimeter Waves, 9, 157
Claude, S., Niranjanan, P., Jiang, F., et al. 2014, Journal of Infrared, Millimeter, and Terahertz Waves, 35, 563
Claude, S., Jiang, F., Niranjanan, P., et al. 2008, SPIE Proceedings, 7020, 70201B
Coutts, G. M. 2011a, IEEE Transactions on Antennas & Propagation, 59, 1902
Coutts, G. M. 2011b, IEEE Transactions on Antennas & Propagation, 59, 1910

Crane, P. C., & Napier, P. J. 1989, Synthesis Imaging in Radio Astronomy, 6, 139
Crawford, A. B., Hogg, D. C. & Hunt, L. E. 1961, Bell System Technical Journal, 40, 1095
D'Addario, L. R. 2003, ALMA Memo 466, https://library.nrao.edu/public/memos/alma/memo466.pdf
D'Addario, L. R., & Stennes, M. J. 1998, SPIE Proceedings, 3357, 691
D'Addario, L. R. 1996, NRAO OVLBI-ES Memo 59, http://library.nrao.edu/public/memos/ovlbi/OVLBI_059.pdf
Deschans, D., Begueret, J.-B., Deval, Y., et al. 2002, ALMA Memo 426, https://library.nrao.edu/public/memos/alma/memo426.pdf
Dhawan, V., 2002, VLA-VLBA Interference Memo 25, http://library.nrao.edu/vlai.shtml
Dolan, G. J., Phillips, T. G., & Woody, D. P. 1979, Applied Phys. Letters, 34, 347
Durand, S. J., & Cotter, T. 2002, SPIE Proceedings, 4845, 63
Ellingson, S. W., Clarke, T. E., Cohen, A., et al. 2009, IEEE Proceedings, 97, 1421
Emerson, D. 2008, ALMA Memo 586, https://library.nrao.edu/public/memos/alma/memo586.pdf
Escoffier, R. P., Comoretto, G., Webber, J. C., et al. 2007, A&A, 462, 801
Emrich, A., Andersson, S., Wannerbratt, M., et al. 2009, 20th International Symposium on Space Terahertz Technology, 174
Ezawa, H., Ishiguro, M., Matsuo, H., et al. 2000, SPIE Proceedings, 4015, 515
Feng, Q.-Q., Li, Z.-C., & Li, G.-Y. 2010, SPIE Proceedings, 7820, 782022
Fisher, R. A., 1930, Statistical Methods for Research Workers, London: Oliver & Boyd
Fujii, Y., Gonzalez, A., Kroug, M., et al. 2013, IEEE Transactions on Terahertz Science & Technology, 3, 39
Gallego, J. D., López-Fernández, I., Diez, C., & Barcia, A. 2004, SPIE Proceedings, 5470, 402
Garcia, J. P., & Alvarez Barros, C. 2012, SPIE Proceedings, 8452, 845232
Gawronski, W. 2008, Modeling and Control of Antennas and Telescopes, Springer Science+Business Media, LLC, New York
Goldsmith, P. F. 2002, Single-Dish Radio Astronomy: Techniques and Applications, 278, 45
Goldsmith, P. F. 1987, International Journal of Infrared and Millimeter Waves, 8, 771
Gonzalez, A., Fujii, Y., Kaneko, K., et al. 2014, SPIE Proceedings, 9153, 91530N
Grahl, B. H., Godwin, M. P., & Schoessow, E. P. 1986, A&A, 167, 390
Granlund, J., Thompson, A. R., & Clark, B. G. 1978, IEEE Transactions on Electromagnetic Compatibility, 20, 451
Greve, A., Kramer, C., & Wild, W. 1998, A&AS, 133, 271
Halverson, N. W., Leitch, E. M., Pryke, C., et al. 2002, ApJ, 568, 38, arXiv: astro-ph/0104489
Hills, R. E., Kurz, R. J., & Peck, A. B. 2010, SPIE Proceedings, 7733, 773317
Hills, R. 2005, ALMA Memo 545, https://library.nrao.edu/public/memos/alma/memo545.pdf
Holdaway, M. A. 2001, ALMA Memo 402, https://library.nrao.edu/public/memos/alma/memo402.pdf
Holmes, B. & Brundadnge, B., 2008, ALMA Back End IPT IF Downconverter Production Specification, BEND-52.06.00.00-003-C-SPE
Houde, M., Akeson, R. L., Carlstrom, J. E., et al. 2001, PASP, 113, 622
Huang, Y. D., Morata, O., Koch, P.M., et al. 2016, SPIE Proceedings, 9911, 99111V
Huggard, P. G., Ellison, B. N., Shen, P., et al. 2002, Electronics Letters, 38, 327
Hunter, T. R. & Kimberk, R. 2015, 26th International Symposium on Space Terahertz Technology, arXiv: 1507.04280
Hunter, T. R., Wilson, R. W., Kimberk, R., et al. 2013, Journal of Astronomical Instrumentation, 2, 1350002, arXiv: 1303.4397
Hunter, T. R., Schwab, F. R., White, S. D., et al. 2011a, PASP, 123, 1087, arXiv:1107.2081
Hunter, T. R., Kimberk, R., Leiker, P. S., Tong, C.-Y. E., & Wilson, R. W. 2011b, SMA Technical Memo 143, arXiv: 1101.1506
Iguchi, S. 2005, PASJ, 57, 643
ITU-R 2013, SA.509-3, http://www.itu.int/rec/R-REC-SA.509-3-201312-I/en

Jackson, J. & Maglathlin, G. W. 2011, EVLA Memo 153
Jewell, P. R. 2002, Single-Dish Radio Astronomy: Techniques and Applications, ASP Conference 278, 313
Jewell, P. R. & Mangum, J. G. 1997, ALMA Memo 170, https://library.nrao.edu/public/memos/alma/memo170.pdf
Johnson, J. B. 1928, Physical Review, 32, 97
Kamazaki, T., Okumura, S. K., Chikada, Y., et al. 2012, PASJ, 64, 29
Kamikura, M., Naruse, M., Asayama, S., et al. 2010, Journal of Infrared, Millimeter, and Terahertz Waves, Volume 31, Issue 6, 697
Kerr, A. R., Pan, S.-K., Claude, S. M. X., et al. 2014, IEEE Transactions on Terahertz Science & Technology, 4, 201, arXiv: 1306.6085
Kesteven, M. 2012, From Antikythera to the Square Kilometre Array: Lessons from the Ancients, 25
Kesteven, M. 1993, VLA Test Memo 169, http://library.nrao.edu/public/memos/vla/test/VLAT_169.pdf
Khudchenko, A., Hesper, R., Baryshev, A., et al. 2012, SPIE Proceedings, 8452, 845214
Kooi, J. W., Chattopadhyay, G., Thielman, M., Phillips, T. G., & Schieder, R. 2000, International Journal of Infrared and Millimeter Waves, 21, 689
Koller, D., Ediss, G. A., Mihaly, L., & Carr, G. L. 2006, International Journal of Infrared and Millimeter Waves, 27, 835
Kraus, J. D. 1986, Radio Astronomy, Second Edition, Cygnus-Quasar Books (Powell, Ohio)
Lamb, J. W. 2003, IEEE Transactions on Antennas and Propagation, 51, 2035
Lamb, James 1992, GBT Memo 74, http://library.nrao.edu/public/memos/gbt/GBT_074.pdf
Lamb, J. W., & Olver, A. D. 1986, IEE Proc. H: Microwaves Antennas & Propagation, 133, 43
Lesurf, J. C. G. 1988, Infrared Physics, 28, 129
Levy, R. 1996, Structural engineering of microwave antennas for electrical, mechanical, and civil engineers, Piscataway, NJ: IEEE Press
Maas, S. 2013, IEEE Microwave Magazine, 14, 34
Mahieu, S., Maier, D., Lazareff, B., et al. 2012, IEEE Transactions on Terahertz Science & Technology, 2, 29
Mangum, J. G., Emerson, D. T., & Greisen, E. W. 2007, A&A, 474, 679, arXiv: 0709.0553
Mangum, J. G., Baars, J. W. M., Greve, A., et al. 2006, PASP, 118, 1257, arXiv: astro-ph/0609329
Martin, D. H., & Puplett, E. 1970, Infrared Physics, 10, 105
Meledin, D. V., Marrone, D. P., Tong, C.-Y. E., et al. 2004, IEEE Transactions on Microwave Theory Techniques, 52, 2338
Miller, M., Graf, U. U., Kinzel, R., et al. 2003, SPIE Proceedings, 4855, 594
Morgan, M., Newton, T., Hayward, B., & Boyd, T. 2007, IEEE MTT-S Int. Microwave Symp., 545
Morris, D., Baars, J. W. M., Hein, H., Steppe, H., & Thum, C. 1988, A&A, 203, 399
Morris, K., Durand, S., & Jackson, J. 2008, XXIX URSI General Assembly, Chicago, USA
Murk, A., Yagoubov, P., Wylde, R., et al. 2010, 21st International Symposium on Space Terahertz Technology, 172
Napier, P. J. 2007, ALMA EDM Document, SYSE-80.04.00.00-018-A-DSN
Napier, P. J. 1999, Synthesis Imaging in Radio Astronomy II, 180, 37
Napier, P. J., Bagri, D. S., Clark, B. G., et al. 1994, IEEE Proceedings, 82, 658
Napier, P. J., Thompson, A. R., & Ekers, R. D. 1983, IEEE Proceedings, 71, 1295
Napier, P. J., & Bates, R. H. T. 1971, International Journal of Engineering Science, 9, 1193
Naruse, M., Ito, T., Sekimoto, Y., et al. 2009, Experimental Astronomy, 24, 89
Nikolic, B., Bolton, R. C., Graves, S. F., Hills, R. E., & Richer, J. S. 2013, A&A, 552, 104, arXiv: 1302.6056
Nikolic, B., Hills, R. E., & Richer, J. S. 2007, A&A, 465, 679, arXiv: astro-ph/0612241
Nyquist, H. 1928, Transactions AIEE, 47, 617
Oliver, B. M. 1965, IEEE Proceedings, 53, 436

Oosterloo, T., Verheijen, M. A. W., van Cappellen, W., et al. 2009, Wide Field Astronomy & Technology for the SKA, 70, arXiv: 0912.0093
Padin, S., Davis, R. J., & Lasenby, A. N. 1987, MNRAS, 224, 685
Paine, S., & Blundell, R. 2004, 15th International Symposium on Space Terahertz Tech., 418
Paine, S., Papa, D. C., Leombruno, R. L., Zhang, X., & Blundell, R. et al. 1994, 5th International Symposium on Space Terahertz Technology, 811
Pan, S.-K., Feldman, M. J., Kerr, A. R., & Timble, P. 1983, Applied Phys. Letters, 43, 786
Pardo, J., Cernicharo, J., & Serabyn, E. 2001, IEEE Transactions on Antennas & Propagation, 49, 1683
Patel, N. A., Wilson, R. W., Primiani, R., et al. 2014, Journal of Astronomical Instrumentation, 3, 1450001
Patel, N. A., & Sridharan, T. K. 2004, SPIE Proceedings, 5496, 639
Penzias, A. A., & Wilson, R. W. 1965, ApJ, 142, 419
Perley, R., Napier, P., Jackson, J., et al. 2009, IEEE Proceedings, 97, 1448, arXiv: 0909.1585
Pospieszalski, M. W. 2005, IEEE Microwave Magazine, 6, 62
Pospieszalski, M. W. 2012, 19th International Conference on Microwave Radar & Wireless Communication, 748
Prestage, R. M., Constantikes, K. T., Hunter, T. R., et al. 2009, IEEE Proceedings, 97, 1382
Rampini, F., & Marchiori, G. 2012, SPIE Proceedings, 8450, 84500T
Randa, J., Lahtinen, J., Camps, A., et al. 2008, NIST Technical Note 1551
Richards, P. L., Shen, T. M., Harris, R. E., & Lloyd, F. L. 1979, Applied Phys. Letters, 34, 345
Rudge, A. W., Milne, K., Olver, A. D., & Knight, P. 1982, The Handbook of Antenna Design, Volume 1, Peter Peregrinus Ltd., London
Rudner, S., & Claeson, T. 1979, Applied Phys. Letters, 34, 711
Rudolf, H., Carter, M., & Baryshev, A. 2007, IEEE Trans. on Antennas & Prop., 55, 2966
Ruze, J. 1966, IEEE Proceedings, 54, 633
Schroeder, D. J. 1987, San Diego, CA, Academic Press, Inc.
Schwab, F. & Hunter, T. R. 2007, GBT PTCS Project Note 59, http://wwwlocal.gb.nrao.edu/ptcs/ptcspn/ptcspn59/pn59.pdf
Sekimoto, Y., Iizuko, Y., Satou, N., et al. 2008, 19th International Symposium on Space Terahertz Technology, 253
Shannon, C.E. 1949, Proceedings of the IRE, 37, 10
Shillue, B., Grammer, W., Jacques, C., et al. 2012, SPIE Proceedings, 8452, 845216
Skinner, S. J., & James, G. L. 1991, IEEE Trans. on Microwave Theory & Techniques, 39, 294
Sørensen, S., & Pontoppidan, K. 2010, 21st International Symposium on Space Terahertz Technology, 121
Sridharan, T. K., Tong, C. E., Saito, M., et al. 2002, 13th International Symposium on Space Terahertz Technology, 545
Srikanth, S., Perley, R., Hayward, R., & Mertely, D. 2005, 28th URSI General Assembly, India
Thompson, A. R., Moran, J. M., & Swenson, G. W. 2007, Interferometry and Synthesis in Radio Astronomy, John Wiley & Sons
Uzawa, Y., Fujii, Y., Gonzalez, A., et al. 2013, Physica C Superconductivity, 494, 189
von Hoerner, S. 1967, AJ, 72, 35
Walker, R. C. 1995, VLBA Scientific Memo 8, https://science.nrao.edu/facilities/vlba/publications/memos/sci/sci08memo.pdf
Wallace, P. T. 1994, Starlink User Note, 100
Wengler, M. J., Woody, D. P., Miller, R. E., & Phillips, T. G. 1985, International Journal of Infrared and Millimeter Waves, 6, 697
Whiteis, P. G., & Mello, M. J. 2012, SPIE Proceedings, 8444, 84445N
Williams, W. F. 1965, Microwave Journal, vol. 8, July issue, 79
Wollack, E. J. 1995, Review of Scientific Instruments, 66, 4305
Woody, D. P., Beasley, A. J., Bolatto, A. D., et al. 2004, SPIE Proceedings, 5498, 30
Wrobel, J. M., & Walker, R. C. 1999, Synthesis Imaging in Radio Astronomy II, 180, 171
Young, A. C. 1991, IAU Colloq. 131: Radio Interferometry. Theory, Techniques, and Applications, ASP Conference Series, 19, 33